Nano Research

ISSN 1998-0124 CN 11-5974/O4
https://doi.org/10.26599/NR.2025.94908023

Research Article

Design of a CuFe metal–organic framework nanozyme to enhance radiotherapy efficacy via mitochondrial oxidative stress amplification and induction of ferroptosis and cuproptosis

Jiansong Han[1,§], Erna Jia[1,2,§], Yi Gao[3,§], Bin Liu[1](✉), Kelong Fan[5,6](✉), Min Luo[4](✉)

[1] Department of Urology, China-Japan Union Hospital of Jilin University, Changchun 130033, China

[2] Department of Gastroenterology, China-Japan Union Hospital of Jilin University, Changchun 130033, China

[3] Department of Cardiology, China-Japan Union Hospital of Jilin University, Changchun 130033, China

[4] Department of Radiation and Medical Oncology, Hubei Key Laboratory of Tumor Biological Behaviors, Hubei Cancer Clinical Study Center, Zhongnan Hospital of Wuhan University, Wuhan 430071, China

[5] CAS Engineering Laboratory for Nanozyme, Key Laboratory of Biomacromolecules (CAS), CAS Center for Excellence in Biomacromolecules, Institute of Biophysics, Chinese Academy of Sciences, Beijing 100101, China

[6] Nanozyme Laboratory in Zhongyuan, Henan Academy of Innovations in Medical Science, Zhengzhou 451163, China

[§] Jiansong Han, Erna Jia, and Yi Gao contributed equally to this work.

Nano Res., **Just Accepted Manuscript** • https://doi.org/10.26599/NR.2025.94908023

https://www.sciopen.com/journal/1998-0124 on Aug. 30, 2025

TABLE OF CONTENTS (TOC)

Design of a CuFe Metal–Organic Framework Nanozyme to Enhance Radiotherapy Efficacy via Mitochondrial Oxidative Stress Amplification and Induction of Ferroptosis and Cuproptosis

Jiansong Han[1,†], Erna Jia[1,2†], Yi Gao[1,†], Bin Liu[1,*], Kelong Fan*, and Min Luo*

Jilin University, Changchun; Chinese Academy of Sciences, Beijing; Wuhan University, Wuhan

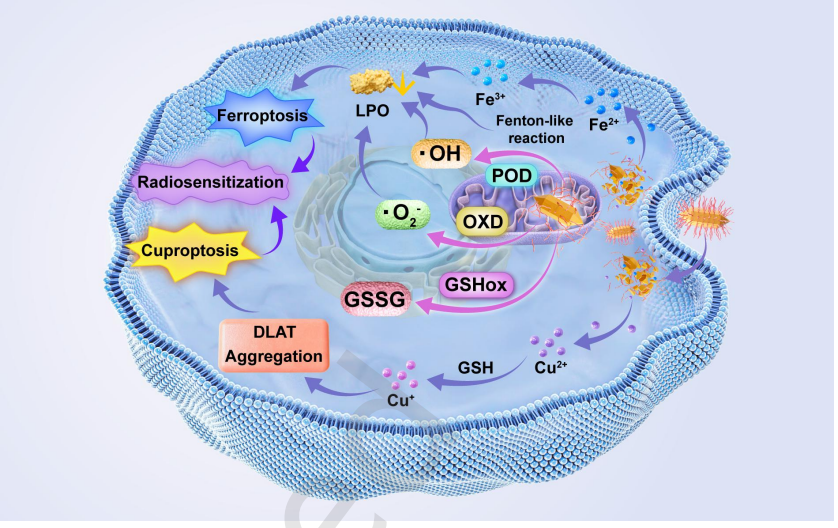

Here a bimetallic MOF nanozyme was constructed for inducing ferroptosis and cuproptosis to improve radiotherapy.

Kelong Fan, http://english.ibp.cas.cn/sourcedb/rck/EN_xsszmA_G/202005/t20200519_341418.html

Nano Research

ISSN 1998-0124 CN 11-5974/O4
https://doi.org/10.26599/NR.2025.94908023

Research Article

Design of a CuFe metal–organic framework nanozyme to enhance radiotherapy efficacy via mitochondrial oxidative stress amplification and induction of ferroptosis and cuproptosis

Jiansong Han[1,§], Erna Jia[1,2,§], Yi Gao[3,§], Bin Liu[1] (✉), Kelong Fan[5,6] (✉), and Min Luo[4](✉)

[1] *Department of Urology, China-Japan Union Hospital of Jilin University, Changchun 130033, China*
[2] *Department of Gastroenterology, China-Japan Union Hospital of Jilin University, Changchun 130033, China*
[3] *Department of Cardiology, China-Japan Union Hospital of Jilin University, Changchun 130033, China*
[4] *Department of Radiation and Medical Oncology, Hubei Key Laboratory of Tumor Biological Behaviors, Hubei Cancer Clinical Study Center, Zhongnan Hospital of Wuhan University, Wuhan 430071 China*
[5] *CAS Engineering Laboratory for Nanozyme, Key Laboratory of Biomacromolecules (CAS), CAS Center for Excellence in Biomacromolecules, Institute of Biophysics, Chinese Academy of Sciences, Beijing 100101, China*
[6] *Nanozyme Laboratory in Zhongyuan, Henan Academy of Innovations in Medical Science, Zhengzhou 451163, China*
[§] *Jiansong Han, Erna Jia, and Yi Gao contributed equally to this work.*

Received: 4 July 2025 / **Revised:** 30 August 2025 / **Accepted:** 30 August 2025

ABSTRACT

Despite advances in radiotherapy (RT), complete tumor eradication remains a clinical challenge, largely due to the insufficient activation of non-apoptotic cell death pathways such as ferroptosis and cuproptosis. To address this, we developed a bimetallic nanozyme, CuFe-MOF-TPP, comprising a CuFe-based metal–organic framework conjugated with triphenylphosphine to enhance RT sensitivity through provoking cuproptosis and ferroptosis. CuFe-MOF-TPP targeted to mitochondria, destroying redox balance by peroxidase-, oxidase-, and glutathione oxidase-like activities. These catalytic functions promoted excessive reactive oxygen species generation and glutathione depletion, leading to oxidative stress in mitochondria. This redox imbalance triggered the generation of ferrous ions, which accelerated lipid peroxidation and subsequently augmented ferroptosis. Concurrently, cuproptosis was promoted through copper ions-mediated aggregation of dihydrolipoamide S-acetyltransferase. Notably, the combination of CuFe-MOF-TPP and RT result in potent tumor suppression via the coordinated delivery of metal ions and spatiotemporally regulated catalytic activity. This strategy offers a promising approach for overcoming radioresistance by synergistically amplifying mitochondrial oxidative stress and activating ferroptosis and cuproptosis, with significant translational potential for clinical cancer therapy.

KEYWORDS

nanozyme, ferroptosis, cuproptosis, radiotherapy, oxidative stress

1. Instructions

The clinical landscape of radiation oncology has evolved considerably driven by revolutionary advances in image-guidance systems and precision drug-delivery techniques[1, 2]. Radiotherapy (RT) represents a non-invasive treatment for tumor suppression, with over half of diagnosed malignancies treated with RT, as a definitive treatment paradigm, an adjuvant protocol, or a palliative therapy [3-5]. Irreversible damage caused by RT irradiation renders cells unable to reproduce and leads to cell death[6]. However, tumor cells are adaptive and can often undergo repair, resulting in incomplete tumor suppression [7-9]. Several novel cell death mechanisms have been discovered recently, including pyroptosis, ferroptosis, autophagy, and cuproptosis, suggesting potential strategies for enhancing the effects of RT [10-14]. Among these, cuproptosis, first described by Tsvetkov et al. in 2022, is characterized by disordered copper metabolism, and is triggered by excess copper ions [15]. This induces aggregation of lipoylated enzymes, especially those involved in the tricarboxylic acid cycle, such as dihydrolipoamide S-acetyltransferase (DLAT), together with depletion of iron-sulfur (Fe-S) cluster proteins [16]. Gu et al. discovered that the elevation of up-regulation of ferredoxin 1 (FDX1) and lipoyl synthase (LIAS) proteins level in residual tumors post RT predict increasing sensitivity of tumors to cuproptosis [12]. Therefore, the development of novel radiation sensitization strategies through activation of cuproptosis pathways

Address correspondence to Bin Liu, liub18@mails.jlu.edu.cn; Kelong Fan, fankelong@ibp.ac.cn; Min Luo, 15172327560@163.com

may have significant potential in overcoming RT resistance. However, intracellular copper concentrations are tightly regulated at specific levels via homeostatic regulatory mechanisms to prevent cellular damage caused by an overload of free copper ions, presenting a challenge to the application of cuproptosis to enhance RT.

Ferroptosis, another form of non-apoptotic cell death, is closely associated with RT, and is considered the primary reason for most of the antitumor effects of RT [17-19]. Ferroptosis is characterized by increased levels of reactive oxygen species (ROS) and reduced levels of glutathione (GSH), leading to a depletion of glutathione peroxidase 4 (GPX4) depletion and an accumulation of lipid peroxides (LPOs) [20, 21]. Ionizing irradiation activates solute carrier family 7 member 11 (SLC7A11) as well as GSH, exhibiting negative feedback to ferroptosis [19]. Thereby, iron-dependent nanoplatforms have been developed for radiosensitization in antitumor treatments by the generation of hydroxyl radicals via the Fenton reaction to trigger ferroptosis. [22, 23]. Furthermore, non-iron-associated strategies have also shown the potential to induce ferroptosis-related radiosensitization [24, 25]. Zinc-copper-based nanoparticles, ZCPO@HA, were reported to induce ferroptosis and cause mitochondrial damage in breast cancer cells through Fenton-like reactions [26-28]. However, both Fenton and Fenton-like reactions require sufficient H_2O_2 as a substrate. Although the intracellular levels of H_2O_2 are higher in tumor cells than in normal cells, this endogenous H_2O_2 is still insufficient to generate adequate amounts of ROS to induce ferroptosis. Fortunately, previous research has revealed that RT promotes mitochondrial respiration, thereby increasing H_2O_2 production, which may offer a solution to the problem of ferroptosis promotion [29]. The combination of ferroptosis nano-inducers and RT would thus provide synergistic effects in improving the outcomes of antitumor therapy.

The use of nanozymes that can overcome the restrictions of redox homeostasis and thus enhance the efficacy of RT has been shown to be effective [30, 31]. Disruption of the redox balance in tumor cells can occur in two ways, namely, elevation of ROS levels to amplify oxidative stress and depletion of GSH to weaken the antioxidant system. Specifically, redox nanozymes that mimic the catalytic properties of natural enzymes such as peroxidase (POD), oxidase (OXD), and other enzymes can protect against highly cytotoxic ROS including organic and inorganic nanozymes [32-35]. On the other hand, glutathione oxidase (GSHox)-mimicking nanozymes can disrupt the redox balance by reducing the levels of GSH [36, 37]. It is worth noting that “all-in-one” nanozymes with multifunctional enzyme-like properties appear to be more effective in the regulation of reactive metabolites [38-40]. Moreover, these “all-in-one” nanozyme with catalytic properties are reported to possess the ability to accelerate ions release [41]. Previous research reported a “pancatalytic therapy” nanozyme with CAT and POD enzyme-mimicking activities which produces cytotoxic ROS to trigger PANoptosis [42, 43]. Nanozymes functioning as oxidoreductases disrupt both redox homeostasis and lipid peroxidation, leading to increased levels of ferroptosis and thus enhancing radiotherapy sensitivity.

In this study, a bimetallic metal-organic framework nanozyme with a triphenylphosphine (TPP) modification, termed CuFe-MOF-TPP, was developed to enhance radiosensitization by inducing both ferroptosis and cuproptosis (Scheme 1). First, CuFe-MOF was fabricated by a reflux method using $Cu(OAc)_2{\cdot}H_2O$ and $Fc(COOH)_2$ as precursors, followed by the conjugation of TPP to $Fc(COOH)_2$ via a carboxyl group to produce the CuFe-MOF-TPP nanozymes. After intravenous administration, the CuFe-MOF-TPP nanozyme can accumulate in tumor tissues due to enhanced permeability and retention (EPR) effects, followed by mitochondrial targeting and induction of its enzymatic activities to disrupt redox homeostasis through dual catalytic actions. Specifically, the CuFe-MOF-TPP nanozyme could generate substantial amounts of $\cdot OH$ and $\cdot O_2^-$ via its POD- and OXD-like activities while consuming GSH via its GSHox-like activity in the mildly acidic tumor microenvironment (TME). Hereby, the oxidative stress was amplified by CuFe-MOF-TPP. During redox reaction, CuFe-MOF-TPP nanozyme released abundant Cu^{2+} and Fe^{2+} ions. Fe^{2+} ions lead to GPX4 depletion and promote LPO, ultimately resulting in ferroptosis. Upregulation of Cu^{2+} could trigger cuproptosis through DLAT aggregation. In addition, the enhanced oxidative stress induced by CuFe-MOF-TPP nanozyme promoted both cuproptosis and ferroptosis. This synergistic interplay between nanozyme-driven redox balance disruption and metal ion toxicity makes the CuFe-MOF-TPP a multimodal amplifier of oxidative stress, simultaneously activating ferroptosis and cuproptosis pathways to overcome radioresistance through redox dysregulation.

2. Result and discussion

2.1 Fabrication and characterization of CuFe-MOF-TPP

CuFe-MOF was synthesized by the reflux method[44]. Next, TPP decoration of CuFe-MOF was performed by an ultrasound-assisted post-synthetic modification (Scheme 1). Transmission electron microscopy (TEM) images showed a uniform rod-like structure of the CuFe-MOF (Figure S1). Atomic force microscopy (AFM) and high-angle annular dark field scanning transmission electron microscopy (HAADF-STEM) confirmed the rod-like structure of the CuFe-MOF-TPP nanozyme (Figure 1A-1C and Figure S2). Elemental mapping confirmed the homogeneous distribution of C, P, Cu, and Fe in the CuFe-MOF-TPP nanozyme, while the presence of C, P, Cu, and Fe signals was confirmed by energy dispersive X-ray spectroscopy (EDS) spectra (Figure 1D and 1E). The zeta potential of the CuFe-MOF-TPP nanozyme was observed to shift from -12.9 mV to -24.5 mV after TPP decoration (Figure 1F). An ultraviolet-visible (UV-Vis) spectrophotometer (Figure 1G) was applied for absorbance measurements of CuFe-MOF nanozyme and CuFe-MOF-TPP nanozyme. Both the Cu 2p and Fe 2p orbitals were present, as shown by X-ray photoelectron spectroscopy (XPS) (Figure 1H). High-resolution XPS analysis of the Cu 2p orbitals showed two component peaks attributed to Cu^{2+} (Figure 1I), one of which showed Cu $2p_{3/2}$ at 934.3 eV and Cu $2p_{1/2}$ at 954.1 eV, while the other showed Cu $2p_{3/2}$ at 934.6 eV and Cu $2p_{1/2}$ at 956.2 eV, both of which were accompanied by satellite peaks. The Fe 2p spectrum attributed to Fe^{2+} demonstrated peaks characteristic of the ferrocene component at 708.0 eV, indicative of Fe $2p_{3/2}$, and at 720.9 eV, representing Fe $2p_{1/2}$, also accompanied by satellite peaks at 710.6 eV and 723.8 eV, respectively (Figure 1J). These results indicated the successful fabrication of CuFe-MOF-TPP.

2.2 Enzyme-like activity evaluation.

Then the multienzyme mimetic activities of CuFe-MOF-TPP nanozyme were evaluated. First, GSH depletion by CuFe-MOF and

CuFe-MOF-TPP was assessed using 5,5'-dithiobis-(2-nitrobenzoic acid) (DTNB). Figure 2A shows the GSH scavenging rates, which were found to be concentration-dependent for both CuFe-MOF and CuFe-MOF-TPP, with over 50% of GSH observed to be consumed at a CuFe-MOF-TPP concentration of 15.6 μg/mL, demonstrating the GSHox-mimicking properties of both CuFe-MOF and CuFe-MOF-TPP. Then, the OXD-like activities were then evaluated using the 3,3',5,5'-tetramethylbenzidine (TMB) colorimetric reaction. As shown in Figure 2B and S3, absorbances at 652 nm increased as the TMB concentration, indicating an increasing generation of ROS. Figure 2C and S4 shows the changes in absorbance in the presence of CuFe-MOF-TPP and CuFe-MOF. The characteristic absorption peak of TPP in CuFe-MOF-TPP appeared at 246 nm. The generation of ROS by CuFe-MOF-TPP was more rapid than that by CuFe-MOF. In addition. Figure 2D and S5 showed ·OH generation from H_2O_2 by CuFe-MOF and CuFe-MOF-TPP measured using TMB kit. It was also found that greater amounts of ROS were produced when the H_2O_2 or TMB concentrations increased (Figure 2E, 2F, S6 and S7). Next, the POD-like activity of CuFe-MOF-TPP, producing ·OH from H_2O_2, was investigated using electron spin resonance (ESR). As shown in Figure 2G, greater ESR signal intensity was observed at pH 6.0 compared to pH 7.4, indicating higher POD-like activity under the mildly acid conditions associated with CuFe-MOF-TPP. Interestingly, the amounts of superoxide anions and hydroxyl radicals generated by CuFe-MOF were higher than those produced by CuFe-MOF-TPP, likely due to the TPP linkage to ferrocene via carboxyl groups which was confirmed by zeta potential and UV-vis spectra measurement, thus occupying active sites and influencing the enzyme activity. Given that remarkable enzyme-like properties, the CuFe-MOF-TPP nanozyme was then evaluated in terms of its ability to induce ferroptosis and cuproptosis. The activity release profiles were investigated in phosphate-buffered saline ((PBS) at different pH values. As shown in Figure 2H and 2I, CuFe-MOF-TPP tended to be more stable under conditions of physiological pH, while showing a significant release of both copper and iron ions at pH 6.5, with a cumulative release of 46.3% Cu^{2+} and 57.7% Fe^{2+} observed after 24 h. Based on the above results, CuFe-MOF-TPP could effectively induce oxidative stress while inhibit regulation of redox balance. During this process, rapid copper and iron ions were released, providing the possibility for induction of cuproptosis and ferroptosis.

2.3 Induction of mitochondrial damage

After confirming that both CuFe-MOF and CuFe-MOF-TPP exhibited satisfactory enzymatic properties, their mitochondrial targeting and ability to induce mitochondrial damage were then investigated. FITC-labeled CuFe-MOF and CuFe-MOF-TPP were co-incubated with CT26 colon carcinoma cells and the effects were observed under confocal laser scanning microscopy (CLSM). As shown in Figure 3A and 3B, stronger FITC fluorescence was observed in CT26 cells treated with CuFe-MOF-TPP, demonstrating the mitochondrial-targeting ability of CuFe-MOF-TPP. The viability of cells treated with varying concentrations of CuFe-MOF and CuFe-MOF-TPP was then assessed. As shown in Figure 3C, CuFe-MOF-TPP showed greater cytotoxicity toward CT26 cells than CuFe-MOF. Next, biocompatibility of CuFe-MOF-TPP was evaluated on MCF-10A cells (Figure S8). Results demonstrated a cell viability exceeding 80% even at a concentration of 100 μg/mL. These results verified that although CuFe-MOF showed higher enzymic activity, greater tumor cell inhibition was achieved by CuFe-MOF-TPP due to mitochondria specific targeting. Moreover, TEM images of CT26 cells treated with CuFe-MOF-TPP demonstrated features of apoptosis or ferroptosis (Figure 3D). The cytoplasm showed obvious focal rarefaction and dissolution. The nucleus was mildly indented. The mitochondria shrank and cristae showed mild dilation with reduced numbers. Rough endoplasmic reticulum was dilated with partial loss of surface ribosomes. Lipid droplets were sparsely scattered. Both autolysosomes and autophagosomes were observed. Furthermore, severe mitochondrial damage was observed, including swelling of the mitochondria with broken cristae. To further elucidate the mechanism underlying mitochondrial dysfunction, LPO levels were quantified using the C11-BODIPY fluorescent probe (Figure 3E). While slight fluorescence representing oxidized C11-BODIPY was observed in Group II and Group III, indicating increased LPO induced by CuFe-MOF-TPP, significant amounts of oxidized C11-BODIPY were found in the group treated with CuFe-MOF-TPP+RT. Collectively, CuFe-MOF-TPP demonstrated superior mitochondrial targeting ability together with RT-potentiated LPO generation.

2.4 Measurement of cuproptosis and ferroptosis

The activation of cuproptosis and ferroptosis pathways by the combination of CuFe-MOF-TPP and RT was then investigated. In cuproptosis, copper ions bind to DLAT, resulting in DLAT aggregation. Compared with Groups I-III where negligible DLAT oligomerization was observed, insoluble DLAT aggregates were found in the group treated with CuFe-MOF+RT (Figure 4A). The strongest fluorescence intensities caused by DLAT aggregation were observed in Group V, indicating that radiosensitization induced by CuFe-MOF-TPP could enhance the levels of cuproptosis (Figure 4B). To examine the levels of ferroptosis resulting from the application of CuFe-MOF-TPP as a radiosensitizer, potential downregulation of GPX4 and LPO accumulation, both hallmarks of ferroptosis, were assessed. As shown in Figure 4C and 4D, GPX4 levels were reduced significantly, while the level of LPO was markedly increased while LPO in Group V. JC-1 staining suggested the presence of more apparent mitochondrial dysfunction induced by CuFe-MOF-TPP+RT than CuFe-MOF+RT, resulting from mitochondria targeting ability of CuFe-MOF-TPP due to TPP decoration (Figure 4E). The expression of the ferroptosis-related marker GPX4 was examined by western blotting, showing marked downregulation of GPX4 in Group V (Figure 4F and 4H). Moreover, CT26 cells treated with CuFe-MOF-TPP+RT showed marked destabilization of the Fe–S cluster protein ferredoxin (FDX1), consistent with the grayscale analysis (Figure 4G). WB analysis of LIAS, Fe-S cluster related proteins, and Lip-DLST, a lipoylated enzyme in the tricarboxylic acid cycle, in each group was measured. As shown in Figure S9, both the protein level of LIAS and Lip-DLST downregulated in Group III, suggesting that CuFe-MOF-TPP lead to cuproptosis. Significant reduction of these cuproptosis-related proteins was observed after CuFe-MOF-TPP+RT treatment. These results suggested the significant induction of both cuproptosis and ferroptosis by CuFe-MOF-TPP in combination with RT.

2.5 Verification of radiosensitization in vitro

Inspired by the above results, the radiosensitization effects of CuFe-MOF-TPP were evaluated in vitro. As CuFe-MOF-TPP possessed both OXD- and POD-mimicking activities, intracellular ROS production was assessed by flow cytometry (FCM) analysis and immunofluorescence staining using dichloro-dihydro-fluorescein diacetate (DCFH-DA) as the probe. As shown in Figure 5A, the average fluorescence intensity in CT26 cells treated with CuFe-MOF-TPP under irradiation was 2.1 times higher than that in the control group. Consistently, strong green fluorescence was observed in Group V (Figure 5B). Next, the rates of cellular apoptosis in all groups were confirmed by FCM using Annexin V-FITC/PI assays (Figure 5C and 5D). Compared with the other groups, the survival rate of cells in Group V was reduced significantly to 53.3%. To investigate the radiosensitization effects of CuFe-MOF-TPP in another cell line, the viability of MB49 cells after various treatments was assessed using CCK-8 assays. This showed that the viability of Group V MB49 cells was reduced to 0.6-fold that of the control group at concentration of 200 μg/mL (Figure S10). Transwell assays were performed to investigate migration in MB49 cells after the different treatments in various treatments. As shown in Figure S11 and S12, neither RT alone nor CuFe-MOF-TPP alone prevented cell migration, while migration was markedly reduced in Group V after the combined treatment, indicating the prevention of tumor cell migration by CuFe-MOF-TPP-enhanced RT. Mitochondrial damage results in impaired ATP production. ATP levels were measured after 12 h of treatment, showing significant decreases in ATP after CuFe-MOF-TPP+RT treatment (Figure 5E).

Elevated ROS can induce immunogenic cell death (ICD). Exposure of damage-associated molecular patterns (DAMPs) including calreticulin (CRT) expression, high mobility group box 1 (HMGB1) secretion was measured. As shown in Figure 5G and 5H, HMGB1 was released from the nuclei of cells in Group V while green fluorescence representing CRT was brightest in Group V. Moreover, dendritic cell (DC) maturation was investigated, indicating that the combined CuFe-MOF-TPP+RT treatment promoted DC maturation significantly (Figure 5F). Hence, CuFe-MOF-TPP enhanced RT to induce DAMPs, triggering ICD, showing the potential of this strategy in immune activation.

2.6 Antitumor effects in vivo

A subcutaneous tumor model was established in mice to investigate in vivo antitumor efficacy (Figure 6A-6C). The biodistribution of CuFe-MOF-TPP nanozyme at various time points post injection was test (Figure S13). Most copper ions accumulated in liver. An apparent accumulation was observed in tumor tissue at 6 h post-injection due to the EPR effect. Following various treatments as shown in Figure 6D, the body weights, tumor volumes, and survival rates of the animals were recorded in all groups. No significant differences among the groups were seen in terms of body weight. Analysis of tumor volumes showed that tumor growth was not controlled in the PBS-treated control group, while Group II treated with RT and Group III treated with CuFe-MOF-TPP showed limited tumor suppression. Group IV, without TPP modification and treated with CuFe-MOF and RT showed optimized tumor inhibition. However, Group V demonstrated the most marked antitumor efficacy with the tumor inhibition rate reaching 95.4%. The survival of mice in Group V was significantly prolonged, indicating the potential antitumor efficacy of CuFe-MOF-TPP-enhanced RT.

Further histological analyses of tumor tissues from the five groups were performed. As shown in Figure 6E, enhanced fluorescent signals representing DLAT oligomerization were observed in Group V, indicative of significant cuproptosis. Reduced GPX4 fluorescent signals revealed that CuFe-MOF-TPP-enhanced RT was effective in triggering ferroptosis. Ki67 immunofluorescence assays indicated the most marked tumor inhibition in Group V. Moreover, it was confirmed that CuFe-MOF-TPP-enhanced RT could induce tumor apoptosis, as shown by Terminal deoxynucleotidyl transferase dUTP Nick-End labeling (Tunel) assays and Hematoxylin and Eosin staining (H&E) staining. Hence, MOF-TPP-enhanced RT showed satisfactory inhibition of tumor growth by induction of cuproptosis and ferroptosis.

A bilateral tumor model was then established to investigate the immune response. First, a primary tumor was established by injection of 2×10^5 CT26 cells into the right hips of the mice, while the second tumor was induced by injection of 2×10^5 CT26 cells into the left hips after 3 days. When the volume of the primary tumor reached approximately 100 mm^3, the mice were divided into five groups and received various treatments. The day of treatment initiation represented day 0 and the volumes of both the primary and second tumors were recorded (Figure 7A-7D). It was found that treatment with RT only and CuFe-MOF-TPP only induced negligible growth suppression of the second tumor, while CuFe-MOF plus RT resulted in obvious tumor inhibition of the non-irradiated distant tumor. It was found that although the distant tumors in Group V were not irradiated, treatment with CuFe-MOF-TPP plus RT performed on the primary tumor resulted in marked suppression of the second tumor, suggesting a significant abscopal effect of CuFe-MOF-TPP plus RT. Moreover, immunofluorescence imaging and quantification of the positive $CD8^+$ area demonstrated significant infiltration of $CD8^+$ T cells in Group V (Figure 7E and 7F). These results show activation of the immune response by CuFe-MOF-TPP plus RT.

Finally, the potential biotoxicity of both CuFe-MOF and CuFe-MOF-TPP was assessed in healthy BALB/c mice by biochemical and hematological analyses, as well as histological analysis of the major organs. As shown in Figure 8A, no significant differences were found among the groups. Furthermore, H&E staining of major organs suggested no noticeable damage (Figure 8B). These results indicated negligible systematic toxicity of CuFe-MOF and CuFe-MOF-TPP.

3. Conclusion

The induction of non-apoptotic cell death, including ferroptosis and cuproptosis, offers a solution to overcoming RT resistance. Thereby, in summary, a novel mitochondrial-targeting nanozyme, CuFe-MOF-TPP, was fabricated for radiosensitization. CuFe-MOF-TPP included three enzymatic activities, namely, POD, OXD, and GSHox, and was more effective in slightly acidic solutions, inducing severe oxidative stress by generating ROS while depleting GSH levels to the antioxidant activity of the cell after localization in the mitochondria. These findings demonstrate that the redox balance in tumors could be disrupted by CuFe-MOF-TPP, triggering abundant release of Cu^{2+} and Fe^{2+} ions. Cu^{2+} bound to DLAT, resulting in DLAT aggregation and the

induction of cuproptosis. Meanwhile, RT amplified this therapeutic cascade by elevating mitochondrial H_2O_2 levels to enhance ROS generation through POD-like catalytic activity, exacerbating oxidative stress to establish a self-reinforcing cuproptosis-ferroptosis cycle. Treatment with CuFe-MOF-TPP plus RT could effectively suppress tumor growth and elicit systemic antitumor immunity, as evidenced by the observed abscopal effect on non-irradiated distant tumors. Consequently, CuFe-MOF-TPP could enhance the effects of RT through the promotion of ferroptosis and cuproptosis, offering a promising antitumor therapeutic approach to overcome RT resistance.

Acknowledgements

This work was financially supported by the National Natural Science Foundation of China (82202312, 82403797), the Jilin Province Health Research Talent Special Project (2022SCZ37) and the Norman Bethune Plan Project of Jilin University (2024B26).

Electronic Supplementary Material: Supplementary material (Experimental section and Figure S1-S4 in the Electronic Supplementary Material) is available in the online version of this article at https://doi.org/10.26599/NR.2025.94908023.

References

[1] Spadea, M. F.;Maspero, M.;Zaffino, P.; Seco, J. Deep learning based synthetic-CT generation in radiotherapy and PET: A review. *Medical Physics* **2021**, *48*, 6537-6566.

[2] Samarasinghe, G.;Jameson, M.;Vinod, S.;Field, M.;Dowling, J.;Sowmya, A.; Holloway, L. Deep learning for segmentation in radiation therapy planning: a review. *Journal of Medical Imaging and Radiation Oncology* **2021**, *65*, 578-595.

[3] Surucu, M.;Ashraf, M. R.;Romero, I. O.;Zalavari, L. T.;Pham, D.;Vitzthum, L. K.;Gensheimer, M. F.;Yang, Y.;Xing, L.;Kovalchuk, N.; Han, B. Commissioning of a novel PET-Linac for biology-guided radiotherapy (BgRT). *Medical Physics* **2024**, *51*, 4389-4401.

[4] Zhu, H.;Chua, M. L. K.;Chitapanarux, I.;Kaidar-Person, O.;Mwaba, C.;Alghamdi, M.;Rodríguez Mignola, A.;Amrogowicz, N.;Yazici, G.;Bourhaleb, Z.;Mahmood, H.;Faruque, G. M.;Thiagarajan, M.;Acharki, A.;Ma, M.;Harutyunyan, M.;Sriplung, H.;Chen, Y.;Camacho, R.;Zhang, Z.; Abdel-Wahab, M. Global radiotherapy demands and corresponding radiotherapy-professional workforce requirements in 2022 and predicted to 2050: a population-based study. *The Lancet Global Health* **2024**, *12*, e1945-e1953.

[5] Meattini, I.;Becherini, C.;Caini, S.;Coles, C. E.;Cortes, J.;Curigliano, G.;de Azambuja, E.;Isacke, C. M.;Harbeck, N.;Kaidar-Person, O.;Marangoni, E.;Offersen, B. V.;Rugo, H. S.;Salvestrini, V.;Visani, L.;Morandi, A.;Lambertini, M.;Poortmans, P.;Livi, L.;Alkner, S.;Bhattacharya, I. S.;Boersma, L.;Callari, M.;Clarke, R. B.;Del Mastro, L.;Ekholm, M.;Gennari, A.;Kirby, A. M.;Kroeze, S.;Malumbres, M.;Vestmø Maraldo, M.;Marta, G. N.;Mjaaland, I.;Morgan, G.;Pistilli, B.;Paluch-Shimon, S.;Rivera, S.;Rottenberg, S.;Saura, C.;Skyttä, T.; Spanic, T. International multidisciplinary consensus on the integration of radiotherapy with new systemic treatments for breast cancer: European Society for Radiotherapy and Oncology (ESTRO)-endorsed recommendations. *The Lancet Oncology* **2024**, *25*, e73-e83.

[6] Guan, X.;Sun, L.;Shen, Y.;Jin, F.;Bo, X.;Zhu, C.;Han, X.;Li, X.;Chen, Y.;Xu, H.; Yue, W. Nanoparticle-enhanced radiotherapy synergizes with PD-L1 blockade to limit post-surgical cancer recurrence and metastasis. *Nature Communications* **2022**, *13*, 2834.

[7] Ma, T. M.;Chu, F.-I.;Sandler, H.;Feng, F. Y.;Efstathiou, J. A.;Jones, C. U.;Roach, M.;Rosenthal, S. A.;Pisansky, T.;Michalski, J. M.;Bolla, M.;de Reijke, T. M.;Maingon, P.;Neven, A.;Denham, J.;Steigler, A.;Joseph, D.;Nabid, A.;Souhami, L.;Carrier, N.;Incrocci, L.;Heemsbergen, W.;Pos, F. J.;Sydes, M. R.;Dearnaley, D. P.;Tree, A. C.;Syndikus, I.;Hall, E.;Cruickshank, C.;Malone, S.;Roy, S.;Sun, Y.;Zaorsky, N. G.;Nickols, N. G.;Reiter, R. E.;Rettig, M. B.;Steinberg, M. L.;Reddy, V. K.;Xiang, M.;Romero, T.;Spratt, D. E.; Kishan, A. U. Local Failure Events in Prostate Cancer Treated with Radiotherapy: A Pooled Analysis of 18 Randomized Trials from the Meta-analysis of Randomized Trials in Cancer of the Prostate Consortium (LEVIATHAN). *European Urology* **2022**, *82*, 487-498.

[8] Wu, Y.;Song, Y.;Wang, R.; Wang, T. Molecular mechanisms of tumor resistance to radiotherapy. *Molecular Cancer* **2023**, *22*, 96.

[9] Falagario, U. G.;Abbadi, A.;Remmers, S.;Björnebo, L.;Bogdanovic, D.;Martini, A.;Valdman, A.;Carrieri, G.;Menon, M.;Akre, O.;Eklund, M.;Nordström, T.;Grönberg, H.;Lantz, A.; Wiklund, P. Biochemical Recurrence and Risk of Mortality Following Radiotherapy or Radical Prostatectomy. *JAMA Network Open* **2023**, *6*, e2332900-e2332900.

[10] Chen, H.;Han, Z.;Luo, Q.;Wang, Y.;Li, Q.;Zhou, L.; Zuo, H. Radiotherapy modulates tumor cell fate decisions: a review. *Radiation Oncology* **2022**, *17*, 196.

[11] Zheng, X.;Jin, X.;Ye, F.;Liu, X.;Yu, B.;Li, Z.;Zhao, T.;Chen, W.;Liu, X.;Di, C.; Li, Q. Ferroptosis: a novel regulated cell

death participating in cellular stress response, radiotherapy, and immunotherapy. *Experimental Hematology & Oncology* **2023**, *12*, 65.

[12] Liao, Y.;Wang, D.;Gu, C.;Wang, X.;Zhu, S.;Zheng, Z.;Zhang, F.;Yan, J.; Gu, Z. A cuproptosis nanocapsule for cancer radiotherapy. *Nature Nanotechnology* **2024**, *19*, 1892-1902.

[13] Li, H.;Yang, T.;Zhang, J.;Xue, K.;Ma, X.;Yu, B.; Jin, X. Pyroptotic cell death: an emerging therapeutic opportunity for radiotherapy. *Cell Death Discovery* **2024**, *10*, 32.

[14] Li, T.;Zhang, Y.;Li, C.;Song, Y.;Jiang, T.;Yin, Y.;Chang, M.;Song, X.;Zheng, X.;Zhang, W.;Yu, Z.;Feng, W.;Zhang, Q.;Ding, L.;Chen, Y.; Wang, S. Microbial Photosynthetic Oxygenation and Radiotherapeutic Sensitization Enables Pyroptosis Induction for Combinatorial Cancer Therapy. *Advanced Materials* **2025**, *n/a*, 2503138.

[15] Tsvetkov, P.;Coy, S.;Petrova, B.;Dreishpoon, M.;Verma, A.;Abdusamad, M.;Rossen, J.;Joesch-Cohen, L.;Humeidi, R.;Spangler, R. D.;Eaton, J. K.;Frenkel, E.;Kocak, M.;Corsello, S. M.;Lutsenko, S.;Kanarek, N.;Santagata, S.; Golub, T. R. Copper induces cell death by targeting lipoylated TCA cycle proteins. *Science* **2022**, *375*, 1254-1261.

[16] Chen, K.;Zhou, A.;Zhou, X.;He, J.;Xu, Y.; Ning, X. Cellular Trojan Horse initiates bimetallic Fe-Cu MOF-mediated synergistic cuproptosis and ferroptosis against malignancies. *Science Advances*, *10*, eadk3201.

[17] Lang, X.;Green, M. D.;Wang, W.;Yu, J.;Choi, J. E.;Jiang, L.;Liao, P.;Zhou, J.;Zhang, Q.;Dow, A.;Saripalli, A. L.;Kryczek, I.;Wei, S.;Szeliga, W.;Vatan, L.;Stone, E. M.;Georgiou, G.;Cieslik, M.;Wahl, D. R.;Morgan, M. A.;Chinnaiyan, A. M.;Lawrence, T. S.; Zou, W. Radiotherapy and Immunotherapy Promote Tumoral Lipid Oxidation and Ferroptosis via Synergistic Repression of SLC7A11. *Cancer Discovery* **2019**, *9*, 1673-1685.

[18] Lyu, M.;Luo, M.;Li, J.;Akakuru, O. U.;Fan, X.;Cao, Z.;Fan, K.; Jiang, W. Personalized Carbon Monoxide-Loaded Biomimetic Single-Atom Nanozyme for Ferroptosis-Enhanced FLASH Radioimmunotherapy. *Advanced Functional Materials* **2023**, *33*, 2306930.

[19] Lei, G.;Zhang, Y.;Koppula, P.;Liu, X.;Zhang, J.;Lin, S. H.;Ajani, J. A.;Xiao, Q.;Liao, Z.;Wang, H.; Gan, B. The role of ferroptosis in ionizing radiation-induced cell death and tumor suppression. *Cell Research* **2020**, *30*, 146-162.

[20] Li, J.;Cao, F.;Yin, H.-l.;Huang, Z.-j.;Lin, Z.-t.;Mao, N.;Sun, B.; Wang, G. Ferroptosis: past, present and future. *Cell Death & Disease* **2020**, *11*, 88.

[21] Cao, J. Y.; Dixon, S. J. Mechanisms of ferroptosis. *Cellular and Molecular Life Sciences* **2016**, *73*, 2195-2209.

[24] Qiao, K.;Huang, Y.;Ning, S.;Lyu, M.;Xie, J.;Zhang, S.;Lu, X.;Yu, Y.;Jiang, W.;Liu, B.;Fan, K.; Liu, T. Camouflaged Nanozymes with Oxidation-Promoting Activities Triggering Ferroptosis for Radio-Immunotherapy. *Advanced Science* **2025**, *n/a*, 2417370.

[25] Chen, Y.;Huang, X.;Hu, R.;Lu, E.;Luo, K.;Yan, X.;Zhang, Z.;Ma, Y.;Zhang, M.; Sha, X. Inhalable biomimetic polyunsaturated fatty acid-based nanoreactors for peroxynitrite-augmented ferroptosis potentiate radiotherapy in lung cancer. *Journal of Nanobiotechnology* **2025**, *23*, 338.

[26] Liu, B.;Chen, X.;Zhu, Y.;Chen, H.;Tan, J.;Yang, Z.;Li, J.;Zheng, P.;Feng, L.;Wang, Q.;Gai, S.;Zhong, L.;Yang, P.;Cheng, Z.; Lin, J. One-Step Symbiosis of Bimetallic Peroxides Nanoparticles to Induce Ferroptosis/Cuproptosis and Activate cGAS-STING Pathway for Enhanced Tumor Immunotherapy. *Advanced Materials* **2025**, *37*, 2500337.

[27] Xiao, Y.;Song, C.;Ye, H.;Li, D.;Shi, J.;Huang, X.;Chen, Q.; Liu, R. A ferroptosis-targeting detachable dissolvable microneedle as a combined therapeutic strategy for radiation-induced oral mucositis. *Chemical Engineering Journal* **2025**, *505*, 158959.

[28] Wang, J.;Jing, Y.;Liu, L.;Xing, P.;Deng, Z.;Zhang, Y.;Wu, X.;Hu, B.;Zhang, C.;Sun, X.;Liu, Y.;Liu, J.;Zhang, J.; Yang, G. Self-Assembled Arachidonic Acid Nanomicelles for Radiation-Induced Ferroptosis to Enhance Tumor Radioimmunotherapy. *Chemical Engineering Journal* **2025**, *507*, 160231.

[29] Taghizadeh-Hesary, F.;Houshyari, M.; Farhadi, M. Mitochondrial metabolism: a predictive biomarker of radiotherapy efficacy and toxicity. *Journal of Cancer Research and Clinical Oncology* **2023**, *149*, 6719-6741.

[30] Zhou, F.;Li, M.;Chen, M.;Chen, M.;Chen, X.;Luo, Z.;Cai, K.; Hu, Y. Redox Homeostasis Strategy for Inflammatory Macrophage Reprogramming in Rheumatoid Arthritis Based on Ceria Oxide Nanozyme-Complexed Biopolymeric Micelles. *ACS Nano* **2023**, *17*, 4358-4372.

[31] Zhao, R.;Zhu, Y.;Feng, L.;Liu, B.;Hu, Y.;Zhu, H.;Zhao, Z.;Ding, H.;Gai, S.; Yang, P. Architecture of Vanadium-Based MXene Dysregulating Tumor Redox Homeostasis for Amplified Nanozyme Catalytic/Photothermal Therapy. *Advanced Materials* **2024**, *36*, 2307115.

[32] Lu, X.;Chen, Z.;Li, Y.;Guo, Y.;Wang, Z.;Zhang, S.;Wang,

Z.;Wang, X.;Gao, S.;Guan, T.;Bai, R.;Guo, M.;Zhou, H.;Gao, X.;Zhang, K.;Cui, Y.;Chen, C.; Wang, Y. Ultrasmall AuCe nanozyme adjuvant boosted ROS for three-pronged tumor immunotherapy. *Nano Today* **2024**, *55*, 102205.

[33] Tang, G.;He, J.;Liu, J.;Yan, X.; Fan, K. Nanozyme for tumor therapy: Surface modification matters. *Exploration* **2021**, *1*, 75-89.

[34] Peng, C.;Pang, R.;Li, J.; Wang, E. Current Advances on the Single-Atom Nanozyme and Its Bioapplications. *Advanced Materials* **2024**, *36*, 2211724.

[35] Nan, F.;Jia, Q.;Xue, X.;Wang, S.;Liu, W.;Wang, J.;Ge, J.; Wang, P. Iron phthalocyanine-derived nanozyme as dual reactive oxygen species generation accelerator for photothermally enhanced tumor catalytic therapy. *Biomaterials* **2022**, *284*, 121495.

[36] Zhu, B.;Wu, J.;Li, T.;Liu, S.;Guo, J.;Yu, Y.;Qiu, X.;Zhao, Y.;Peng, H.;Zhang, J.;Miao, L.; Wei, H. A Glutathione Peroxidase-Mimicking Nanozyme Precisely Alleviates Reactive Oxygen Species and Promotes Periodontal Bone Regeneration. *Advanced Healthcare Materials* **2024**, *13*, 2302485.

[37] Wu, C.;Xu, D.;Ge, M.;Luo, J.;Chen, L.;Chen, Z.;You, Y.;Zhu, Y.-x.;Lin, H.; Shi, J. Blocking glutathione regeneration: Inorganic NADPH oxidase nanozyme catalyst potentiates tumoral ferroptosis. *Nano Today* **2022**, *46*, 101574.

[38] Li, X.;Zhang, X.;Song, L.;Li, Y.;Liu, A.;Li, L.;Nešić, M. D.;Li, D.;Peng, L.;Wang, C.; Lin, Q. Nanozyme as Tumor Energy Homeostasis Disruptor to Augment Cascade Catalytic Therapy. *ACS Nano* **2024**, *18*, 34656-34670.

[39] Cheng, Y.;Xia, Y.-D.;Sun, Y.-Q.;Wang, Y.; Yin, X.-B. "Three-in-One" Nanozyme Composite for Augmented Cascade Catalytic Tumor Therapy. *Advanced Materials* **2024**, *36*, 2308033.

[40] Ma, Z.;Foda, M. F.;Liang, H.;Zhao, Y.; Han, H. In Situ Nanozyme-Amplified NIR-II Phototheranostics for Tumor-Specific Imaging and Therapy. *Advanced Functional Materials* **2021**, *31*, 2103765.

[41] Wang, Z.;Wang, X.;Dai, X.;Xu, T.;Qian, X.;Chang, M.; Chen, Y. 2D Catalytic Nanozyme Enables Cascade Enzyodynamic Effect-Boosted and Ca2+ Overload-Induced Synergistic Ferroptosis/Apoptosis in Tumor. *Advanced Materials* **2024**, *36*, 2312316.

[42] Wang, S.;Liu, X.;Wu, Y.;Huang, H.;Song, X.;Feng, W.;Dai, X.; Chen, Y. Defect-engineered sonopiezoelectric nanosheets enable sacrificial-agent-free hydrogen peroxide self-cycling for enhanced pancatalytic therapy. *Cell Biomaterials* **2025**, 10.1016/j.celbio.2025.100101.

[43] Huang, H.; Chen, Y. Catalytic biomaterials, catalytic biology and catalytic medicine. *Science Bulletin* **2025**, *70*, 1554-1558.

[44] Zheng, Z.;Nguyen, H. L.;Hanikel, N.;Li, K. K.-Y.;Zhou, Z.;Ma, T.; Yaghi, O. M. High-yield, green and scalable methods for producing MOF-303 for water harvesting from desert air. *Nature Protocols* **2023**, *18*, 136-156.

Nano Research
ISSN 1998-0124 CN 11-5974/O4
https://doi.org/10.26599/NR.2025.94908023

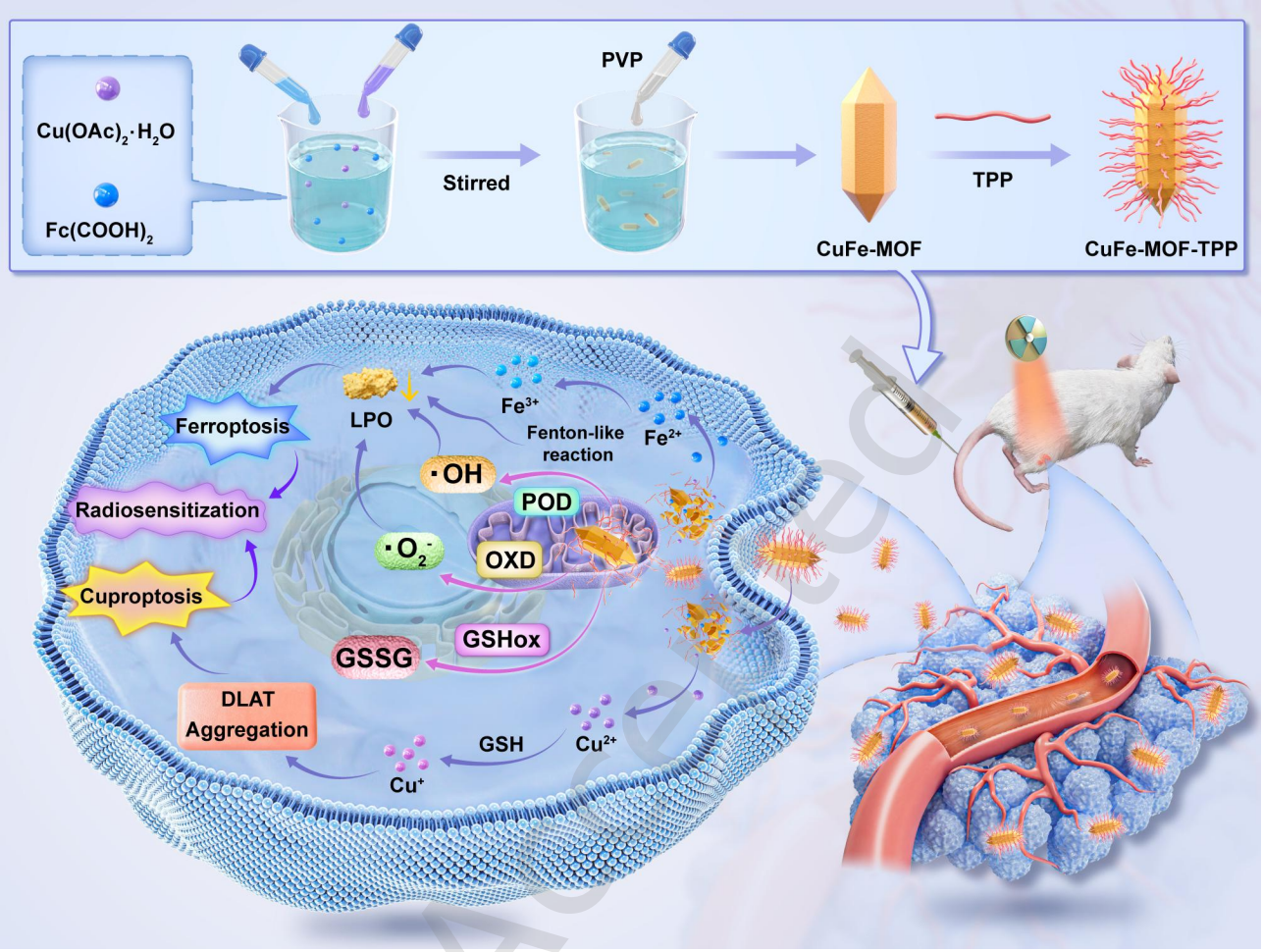

Scheme 1. Schematic illustration of CuFe-MOF-TPP-mediated induction of ferroptosis and cuproptosis for radiotherapy enhancement.

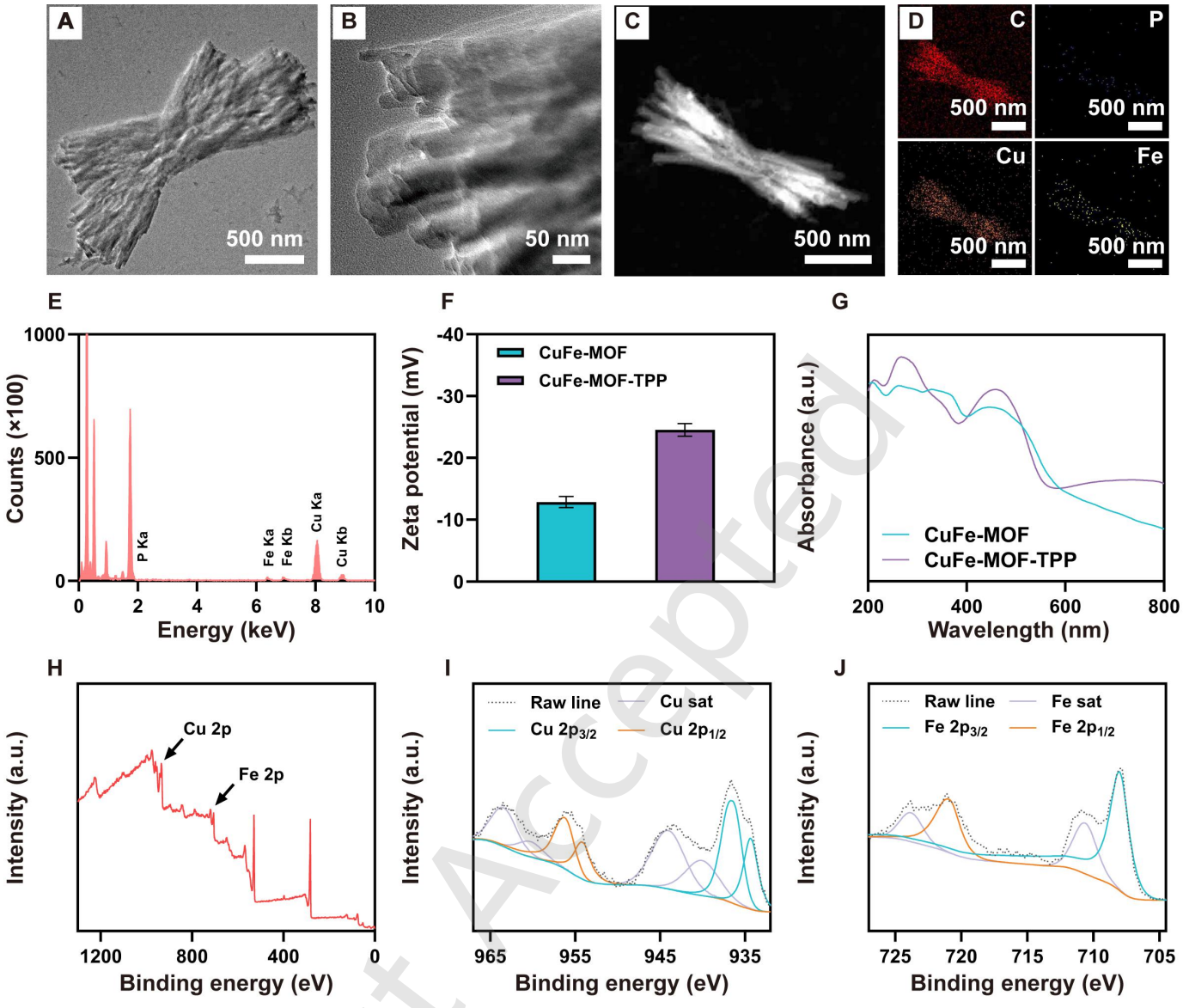

Figure 1. Characterization of CuFe-MOF-TPP. A-B) TEM images of CuFe-MOF-TPP. C-D) HAADF-STEM images and elemental mapping of CuFe-MOF-TPP. E) EDS spectrum of CuFe-MOF-TPP. F) Zeta potential changes in CuFe-MOF and CuFe-MOF-TPP. G) UV-visspectra of CuFe-MOF and CuFe-MOF-TPP. H-J) Full XPS spectrum and Cu 2p and Fe 2p spectra of CuFe-MOF-TPP, respectively.

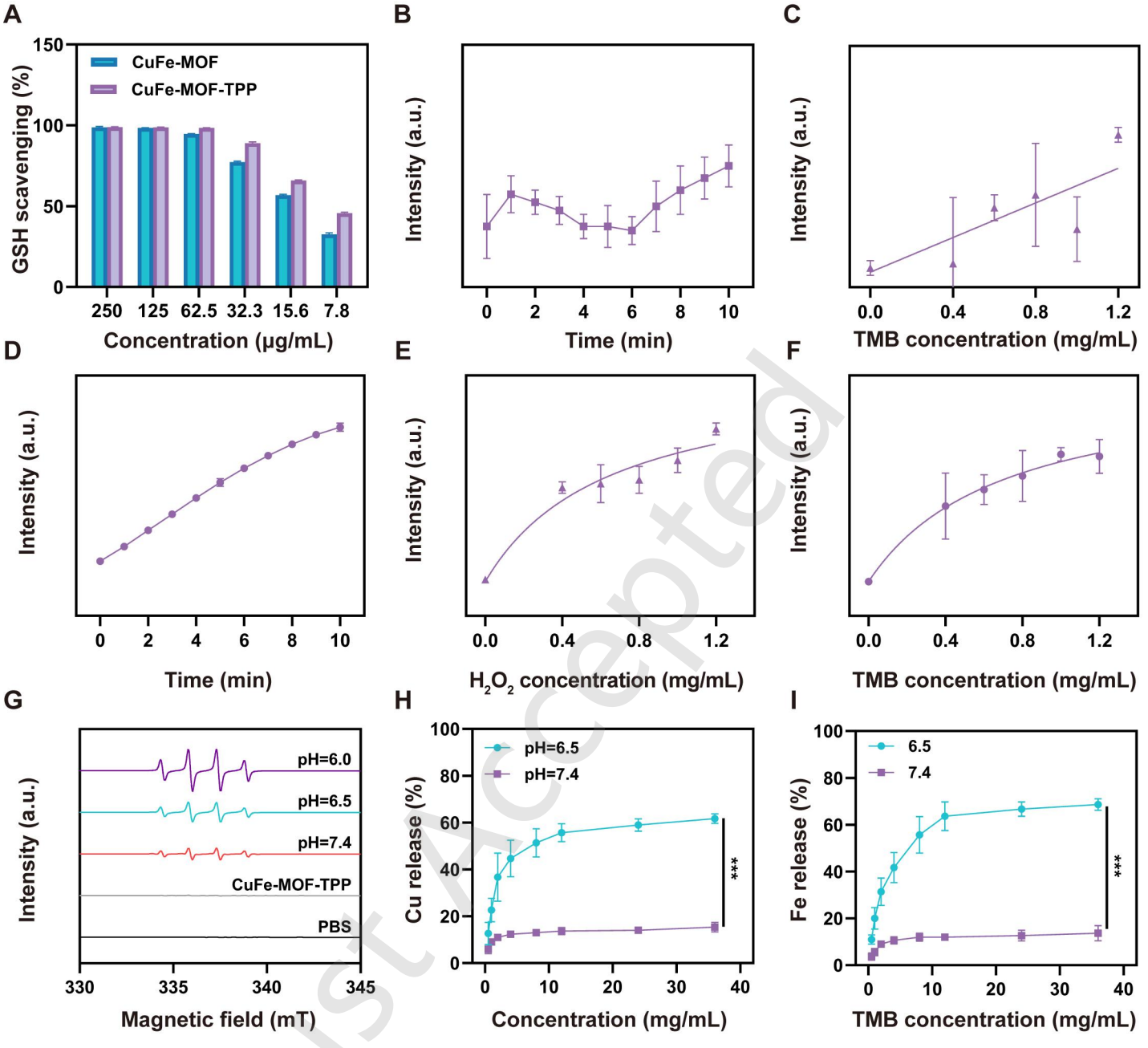

Figure 2. Evaluation of CuFe-MOF-TPP catalytic performance. A) GSH consumption of CuFe-MOF and CuFe-MOF-TPP at different concentrations. B-C) OXD-like activities of CuFe-MOF-TPP. B) Absorbances at 652 nm of CuFe-MOF-TPP detected by TMB. C) Absorbances at 652 nm of CuFe-MOF-TPP using TMB at various TMB concentrations. D-F) POD-like activities of CuFe-MOF-TPP. D) Absorbances at 652 nm of CuFe-MOF-TPP detected by TMB at different times in the presence of H_2O_2. E) Absorbance at 652 nm of CuFe-MOF-TPP detected by TMB under different H_2O_2 concentrations. F) Absorbances of different TMB concentrations in the presence of H_2O_2. G) ESR spectra of •OH trapped by DMPO generated from CuFe-MOF-TPP at different pH values. H-I) Cumulative release curves of Cu and Fe from CuFe-MOF-TPP in PBS at different pH values. n=3. a.u.: arbitrary unit.

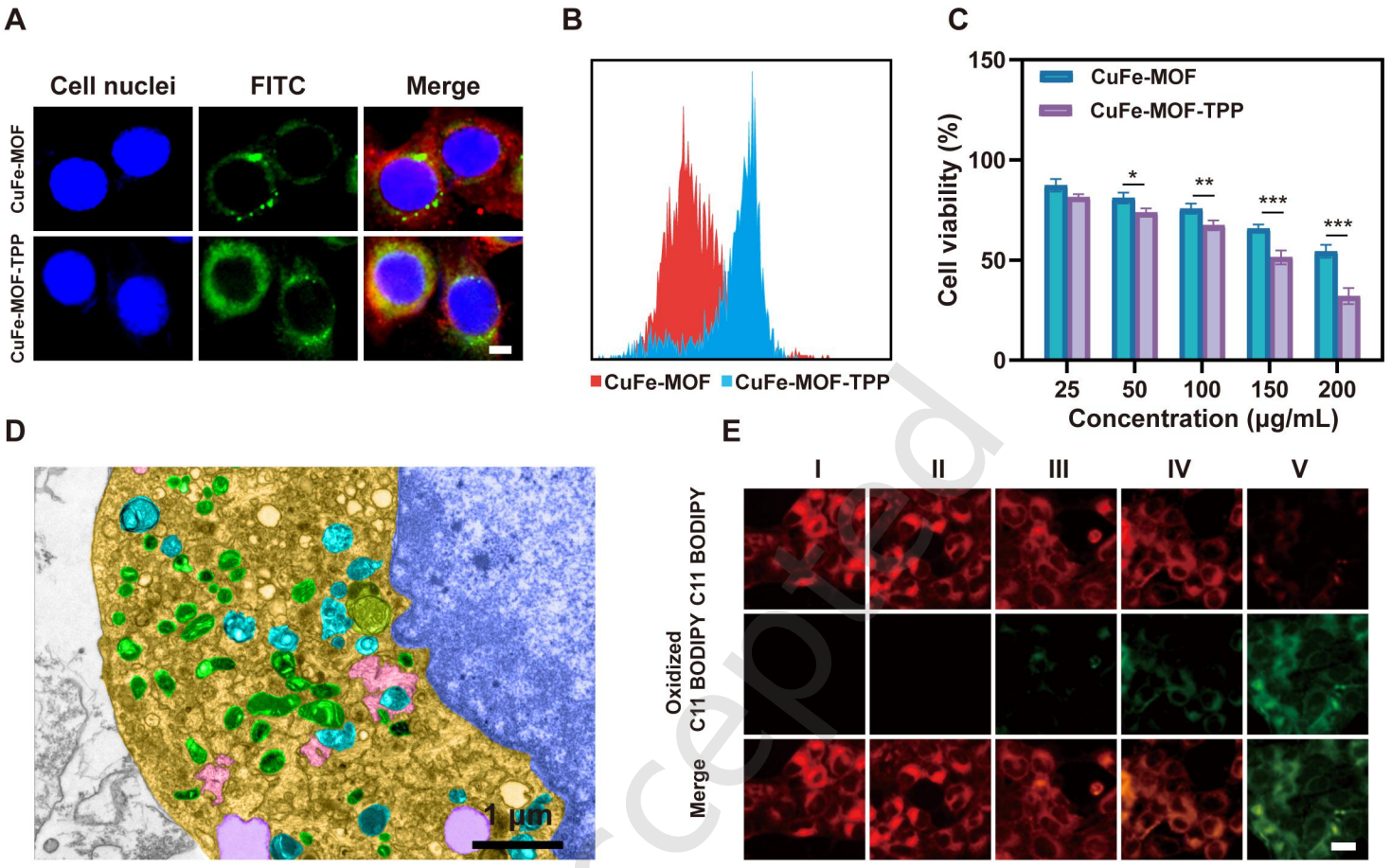

Figure 3. CuFe-MOF-TPP induce mitochondrial damage. A) CLSM images showing co-localization of CuFe-MOF and CuFe-MOF-TPP with mitochondria. Scale bar: 10 μm. B) Flow cytometry analysis of FITC-labeled CuFe-MOF and CuFe-MOF-TPP. C) Viability of CT26 cells after treatment with varying concentrations of CuFe-MOF and CuFe-MOF-TPP. D) TEM images of CT26 cells treated with CuFe-MOF-TPP. Yellow: cytoplasm; Blue: cell nuclei; Purple: lipid droplets; Green: mitochondria; Red: rough endoplasmic reticulum; Teal: autolysosomes; Lime green: autophagosomes. E) CLSM images of treated CT26 cells stained with C11-BODIPY581/591. Scale bar: 10 μm. Group descriptions: I, Control; II, RT; III, CuFe-MOF-TPP; IV, CuFe-MOF +RT; V, CuFe-MOF-TPP+RT. Data are presented as mean ± SD (n=3), Student's t-test, *$p < 0.05$, **$p < 0.01$, ***$p < 0.001$.

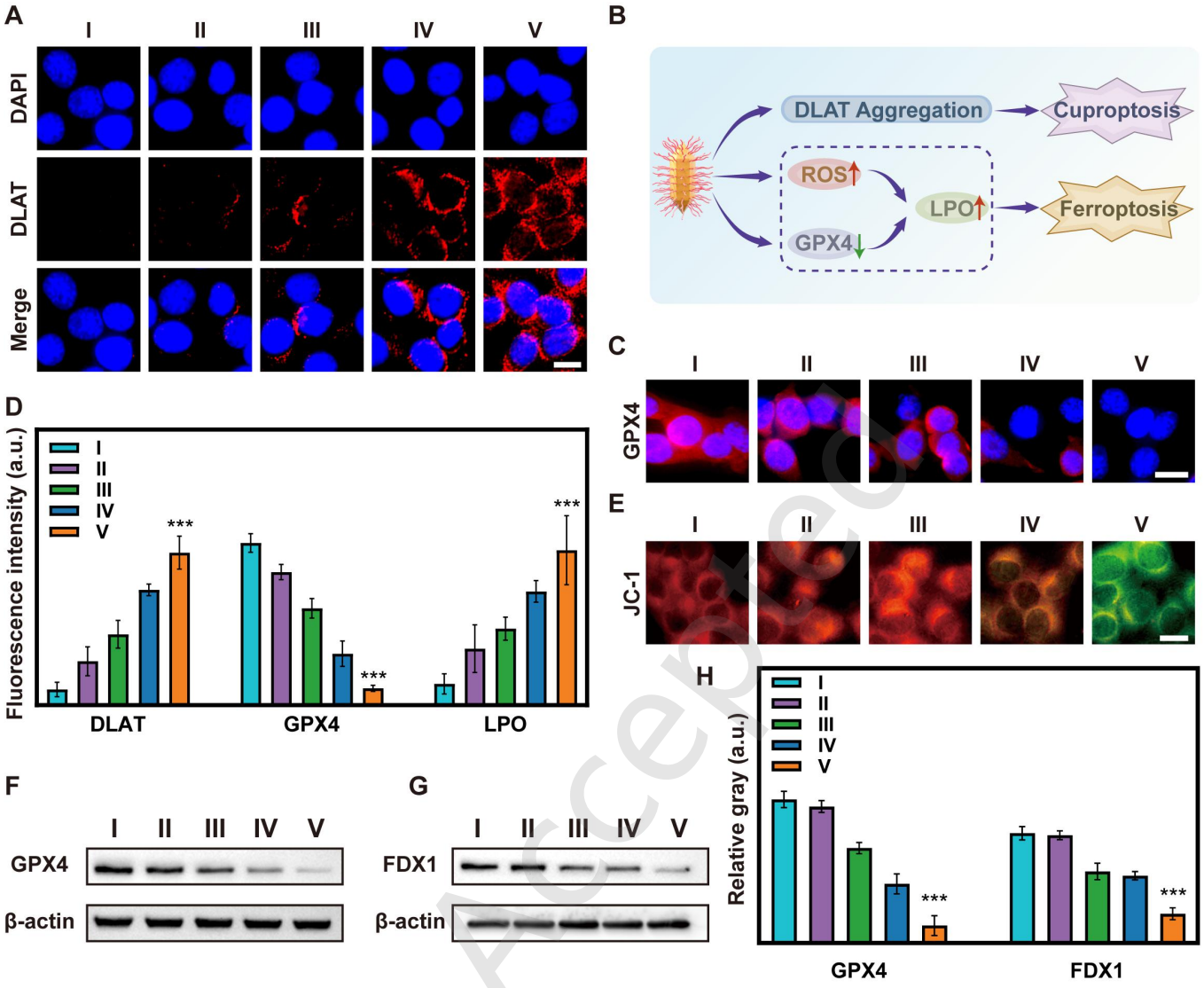

Figure 4. CuFe-MOF-TPP enhances RT-induced cuproptosis and ferroptosis. A) CLSM images of DLAT in CT26 cells after different treatments. Scale bar: 10 μm. B) Schematic diagram of the mechanisms of cuproptosis and ferroptosis. C) CLSM images of GPX4 in CT26 cells after different treatments. Scale bar: 10 μm. D) Fluorescence intensities in CT26 cells after different treatments. E) CLSM images showing changes in mitochondrial membrane potentials. Scale bar: 10 μm. F-G) Western blotting analysis of the expression of F) GPX4 and G) FDX1. H) Quantification of the expression levels in the different treatment groups. Group descriptions: I, Control; II, RT; III, CuFe-MOF-TPP; IV, CuFe-MOF +RT; V, CuFe-MOF-TPP +RT. Data are presented as mean ± SD (n=3), one-way ANOVA, *$p < 0.05$, **$p < 0.01$, ***$p < 0.001$.

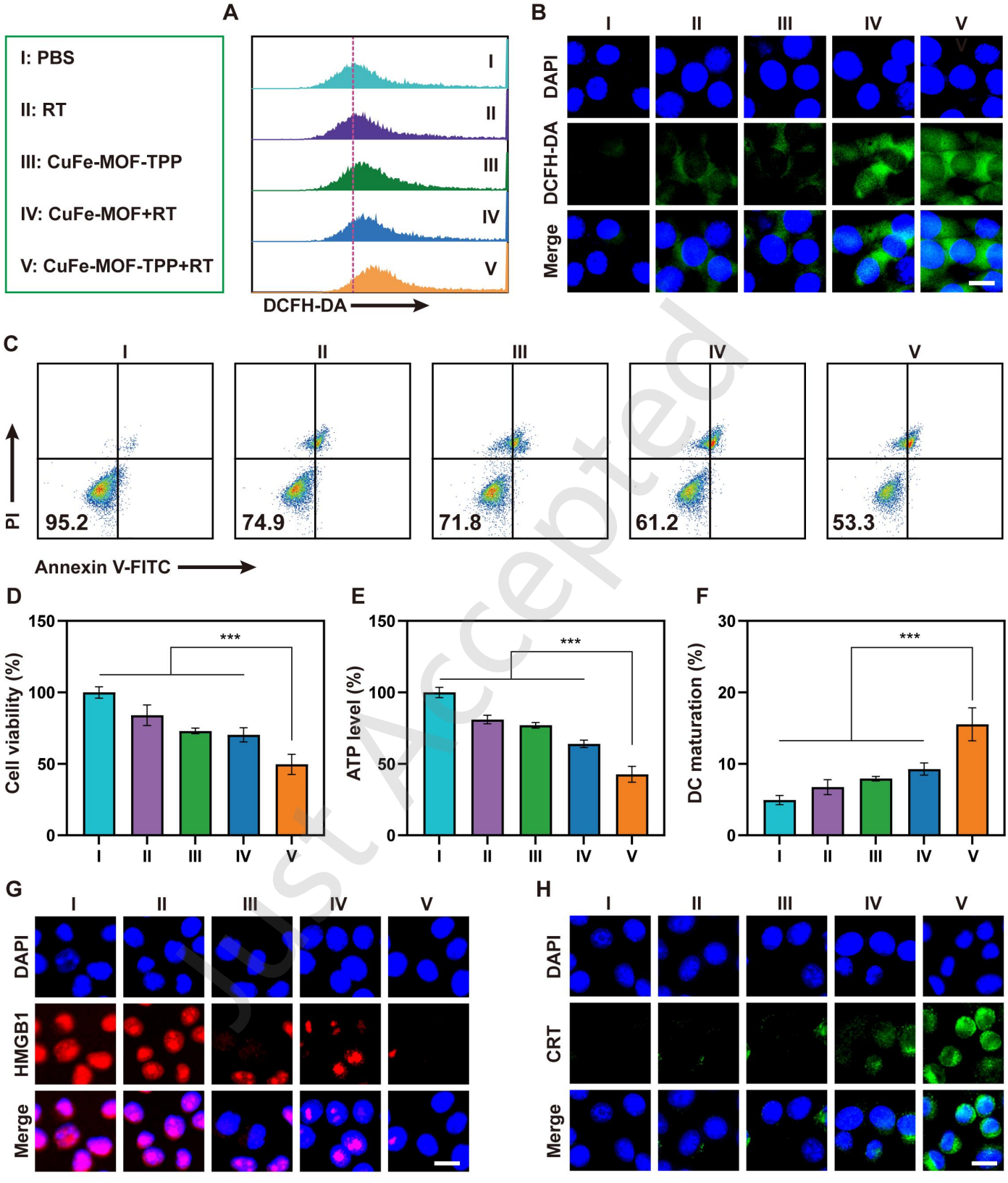

Figure 5. CuFe-MOF-TPP enhanced the effects of RT *in vitro*. A) FCM analysis of ROS generation in CT26 cells. B) Representative CLSM images of intracellular ROS generation. Scale bar: 10 μm. C) FCM analysis of cell apoptosis in the different treatment groups. D) Cytotoxicity of CT26 cells after different treatments. E) Levels of intracellular ATP. F) Quantification of dendritic cell maturation. G-H) CLSM images of G) HMGB1 and H) CRT immunofluorescence staining after various treatments. Scale bar: 10 μm. Group descriptions: I, Control; II, RT; III, CuFe-MOF-TPP; IV, CuFe-MOF +RT; V, CuFe-MOF-TPP+RT. Data are presented as mean ± SD (n=3), one-way ANOVA, *$p < 0.05$, **$p < 0.01$, ***$p < 0.001$.

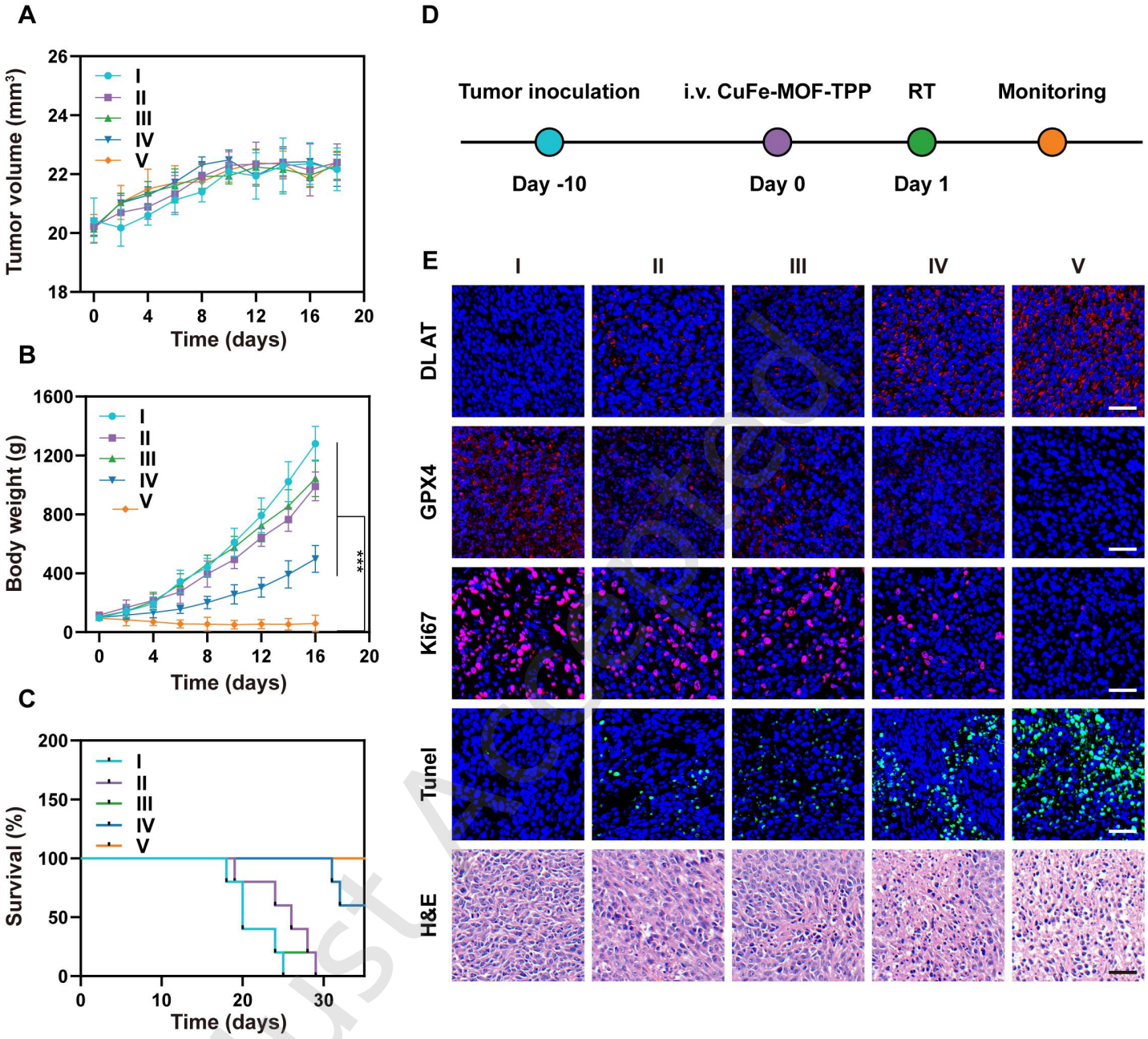

Figure 6. Evaluation of antitumor efficacy in vivo. A) Tumor growth curves. B) Changes in body weight. C) Survival curves. D) Schematic diagram showing treatment procedure. E) DLAT, GPX4, Tunel, Ki67, and H&E staining of tumors from the different treatment groups. Scale bar: 50 μm. Group descriptions: I, Control; II, RT; III, CuFe-MOF-TPP; IV, CuFe-MOF +RT; V, CuFe-MOF-TPP+RT. Data are presented as mean ± SD (n=5), two-way ANOVA, *p < 0.05, **p < 0.01, ***p < 0.001.

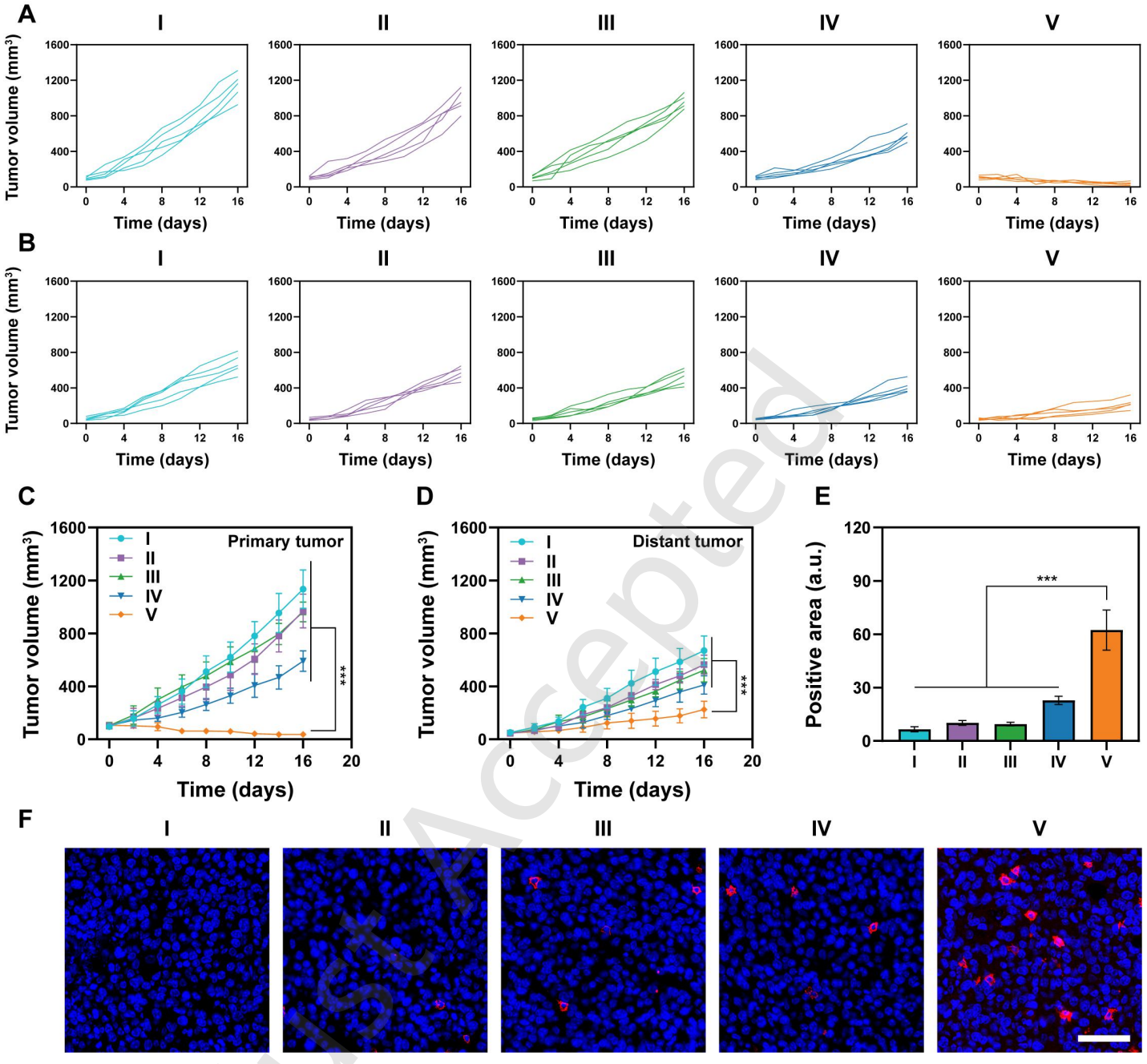

Figure 7. Inhibition of primary and distant tumor growth. A) Primary tumor growth curve. B) Distant tumor growth curve. C-D) Growth curves of the primary tumor C) and distant tumor D) in the different treatment groups. E) Quantitative analysis of the $CD8^+$ T-cell-positive area. F) $CD8^+$ T-cell staining of distant tumors in the different groups. Scale bar: 50 μm. Group descriptions: I, Control; II, RT; III, CuFe-MOF-TPP; IV, CuFe-MOF +RT; V, CuFe-MOF-TPP+RT. Data are presented as mean ± SD (n=5), two-way ANOVA, *$p < 0.05$, **$p < 0.01$, ***$p < 0.001$.

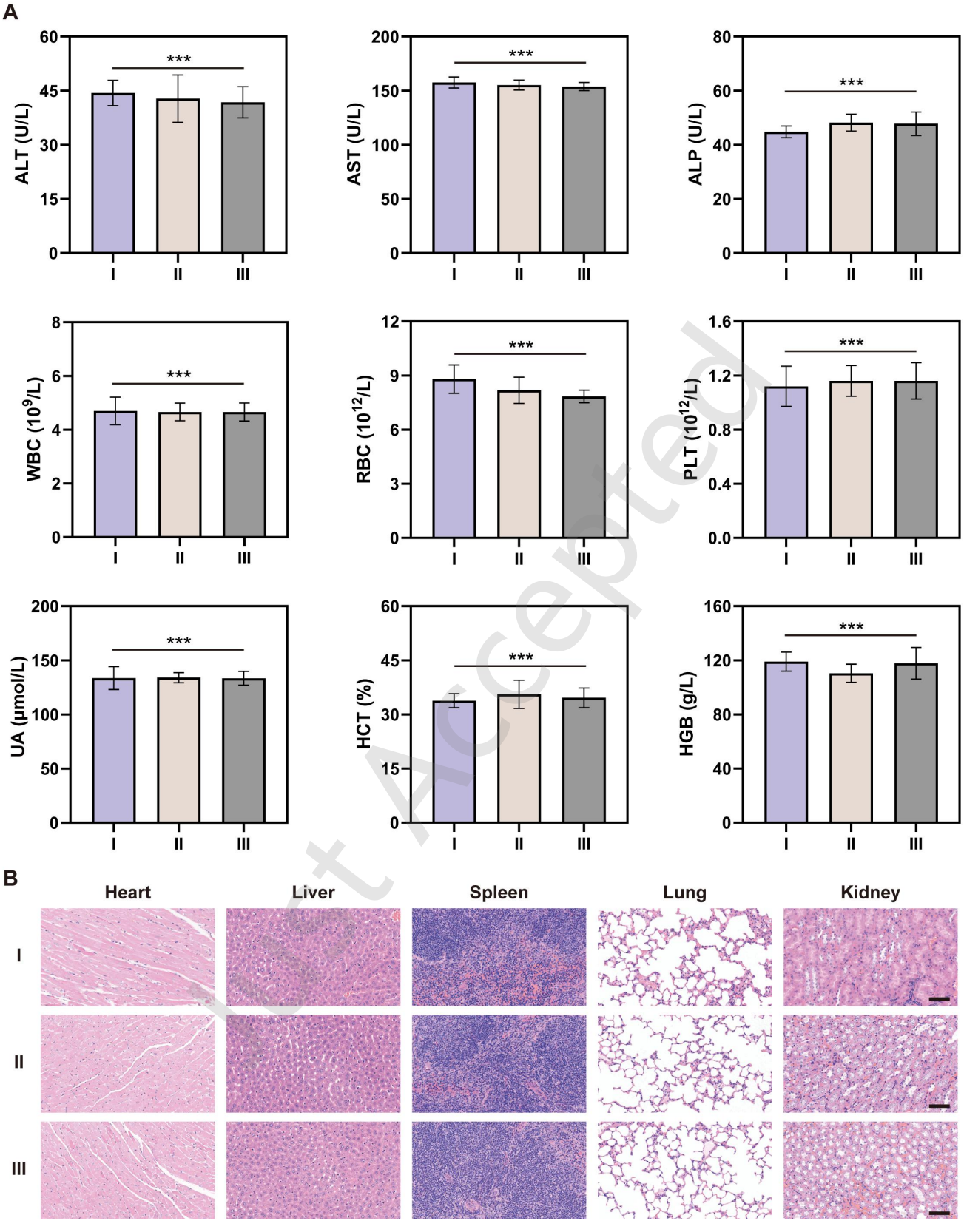

Figure 8. Evaluation of biocompatibility. A) Biochemical analyses and hematological indices of mice on day 15 after injection. Alanine aminotransferase (ALT), aspartate aminotransferase (AST), alkaline phosphatase (ALP), white blood cells (WBC), red blood cells (RBC), platelets (PLT), uric acid (UA), hematocrit (HCT), and hemoglobin (HGB). B) Images of H&E-stained major organs from mice on day 15 after injection. Scale bar: 50 μm. Group description: I, PBS; II, CuFe-MOF; III, CuFe-MOF-TPP. Data are presented as mean ± SD (n=5), two-way ANOVA, *$p < 0.05$, **$p < 0.01$, ***$p < 0.001$

Electronic Supplementary Material

Design of a CuFe metal–organic framework nanozyme to enhance radiotherapy efficacy via mitochondrial oxidative stress amplification and induction of ferroptosis and cuproptosis

Jiansong Han[1,§], Erna Jia[1,2,§], Yi Gao[3,§], Bin Liu[1] (✉), Kelong Fan[5,6] (✉), and Min Luo[4](✉)

[1] *Department of Urology, China-Japan Union Hospital of Jilin University, Changchun 130033, China*
[2] *Department of Gastroenterology, China-Japan Union Hospital of Jilin University, Changchun 130033, China*
[3] *Department of Cardiology, China-Japan Union Hospital of Jilin University, Changchun 130033, China*
[4] *Department of Radiation and Medical Oncology, Hubei Key Laboratory of Tumor Biological Behaviors, Hubei Cancer Clinical Study Center, Zhongnan Hospital of Wuhan University, Wuhan 430071 China*
[5] *CAS Engineering Laboratory for Nanozyme, Key Laboratory of Biomacromolecules (CAS), CAS Center for Excellence in Biomacromolecules, Institute of Biophysics, Chinese Academy of Sciences, Beijing 100101, China*
[6] *Nanozyme Laboratory in Zhongyuan, Henan Academy of Innovations in Medical Science, Zhengzhou 451163, China*
[§] *Jiansong Han, Erna Jia, and Yi Gao contributed equally to this work.*

Supporting information to https://doi.org/10.26599/NR.2025.94908023

Experimental Section

1. Materials

   Copper (II) acetate monohydrate ($Cu(OAc)_2 \cdot H_2O$, 98%), 1,1'-Ferrocenedicarboxylic acid ($Fc(COOH)_2$, 98%), polyvinyl pyrrolidone (PVP, K10) N,N-Dimethylformamide (DMF, DMF), 5-carboxy triphenylphosphine (TPP, 97%) were purchased from Sigma-Aldrich. All the chemicals were used without further purification.

2. Synthesis procedure of CuFe-MOF-TPP nanozyme

   1.2 mM $Cu(OAc)_2 \cdot H_2O$, 1.2 mM $Fc(COOH)_2$, and 3.503 g PVP were dissolved in 24 mL DMF under sonication at room temperature for 30 minutes. Then the solution was kept at 120 ℃ in a metal bath under reflux condensation under continuous stirring for 3 h. After the reaction completed and cooled down to room temperature, the mixture was centrifugated at 10000 rpm and the supernatant was removed. Next the precipitate was washed using DMF for three times excess residual to obtain CuFe-MOF nanozyme.

   Next, 60 mg CuFe-MOF nanozyme was dispersed in 3 mL double distilled (DD) H_2O under sonication for 5 min. Subsequently, 2 mg TPP was dispersed in 500 μL DD H_2O and was added dropwisely to the CuFe-MOF dispersion. After stirring for 3 h, the reaction mixture was centrifuged at 10000 rpm for 10 min, following purification with DD H_2O for 3 times. Finally, the participate was freeze-dried to obtain CuFe-MOF-TPP nanozyme.

3. Sample Characterization

   Transmission electron microscopy (TEM) images, elemental mapping and energy dispersive x-ray spectroscopy (EDS) spectrum were obtained on FEI Tecnai F20. The Zeta potential and size distribution were tested on a dynamic light scattering instrument (DLS, Nano-2 s90, Malvern) at room temperature. X-ray photoelectron spectroscopy (XPS) was recorded by Thermal Fisher ESCALAB 250Xi. Electron spin resonance (ESR) measurements were conducted on a Bruker EMXplus. Absorption spectrum was assessed on UV-visible-near-infrared spectrophotometer (UV-VIS-NIR, Shimadzu UV3600).

4. Assessment of biodegradability performance

   1 mg of CuFe-MOF-TPP nanoparticles were dispersed in 2 mL PBS buffers with various pH values (7.4 and 6.5) at 37 ℃ under stirring. Then supernatant was collected at different time points and the concentrations of copper ions and ferrous ions were determined by ICP-OES.

5. ESR measurements. 100 μL of 5,5-dimethyl-1-pyrroline-N-oxide (DMPO)

To detect the hydroxyl radical production, 100 μL CuFe-MOF-TPP (5 mg/mL) and 10 μL H_2O_2 (10 M) were dissolved in PBS buffer. 5,5-Dimethyl-1-pyrroline N-oxide (DMPO) was added as trapping agent. Next, 100 μL CuFe-MOF-TPP (5 mg/mL) were dispersed in PBS buffer with the assistance of DMPO for superoxide anions investigation. ESR signals were evaluated using ESR measurements.

6. Peroxidase (POD), oxidase (OXD) and glutathione oxidase (GSHox) like activity evaluation

The POD-like activity was measured by 3,5,3,5-tetramethylbenzidine (TMB) as a probe for hydroxyl radical production. CuFe-MOF-TPP was added to H_2O_2 solution, then UV-visible absorption spectra at 652 nm of the supernatant were assessed.

Next, to measure the OXD-like activity, TMB was added in CuFe-MOF-TPP solution for superoxide radical generation evaluation. The absorbance was recorded after a certain reaction time using a UV-vis spectrophotometer (652 nm).

The GSHox-mimicking activity was measured using 5,5'-dithiobis-2-nitrobenzoicacid (DTNB). Different concentrations of CuFe-MOF and CuFe-MOF-TPP was mixed with 1 mM GSH. After a certain reaction time, the solution was mixed with DTNB solution. Finally, the absorbance was measured using a UV-vis spectrophotometer.

7. Cell culture

Murine bladder cell line (MB49) and murine colon cell line (CT26) were obtained from Cell Bank, Shanghai Institutes for Biological Sciences, Chinese Academy of Sciences. MB49 and CT26 cells were cultivated in DMEM and RPMI-1640 supplemented with 10% Fetal Bovine Serum respectively. All cells were cultured at 37 ℃ in a 5% CO2 atmosphere.

8. Cell viability

CT26 cells or MB49 cells were seeded in 96-well plates and incubated for 24 h. Next the cell culture medium was replaced with fresh medium with CuFe-MOF and CuFe-MOF-TPP at various concentrations. After 12 h, cells were washed and Cell Counting Kit 8 reagent was added. A microplate reader was used for absorbance measurements.

9. Cellular uptake and localization.

Both CuFe-MOF and CuFe-MOF-TPP nanozymes were labeled with FITC. Next, CT26 cells were seeded in confocal dishes and cultivated overnight. After replacing the medium with fresh medium containing FITC labeled CuFe-MOF and CuFe-MOF-TPP, the fluorescence distribution was observed using confocal laser scanning microscope (CLSM). Next, the fluorescence intensity of FITC was investigated using FCM.

10. Observation of cell morphology using TEM imaging

CT26 cells were seeded in 6-well plates and cultured for 24 h. The cells were then treated with 6 Gy radiotherapy (RT) after CuFe-MOF-TPP were added in medium and incubated for an additional 24 h. Subsequently, cells were collected, resuspended in 2.5% glutaraldehyde fixative and fixed overnight. Following fixation, samples were dehydrated through a graded ethanol series, embedded in paraffin, and sectioned. Ultrastructural analysis was performed using transmission electron microscopy (TEM).

11. Flow cytometry analysis of the cell apoptosis

CT26 cells were seeded in 6-well plates and cultured for 24 h. Cells were treated with different groups (Group I: Control; Group II: RT (6 Gy); Group III: CuFe-MOF-TPP (50 μg/mL); Group IV CuFe-MOF (49 μg/mL)+RT (6 Gy); Group V CuFe-MOF-TPP(50 μg/mL)+RT (6 Gy)) and incubated for 24 h. Then all cells were collected by centrifugation and rinsed several times with PBS, followed by staining with Annexin-V-FITC/PI and analyzed by FCM.

12. Detection of ROS generation in cells

After cells were seeded in 6-well plates, CT26 cells were treated with the following condition: Group I: Control; Group II: RT (6 Gy); Group III: CuFe-MOF-TPP (50 μg/mL); Group IV CuFe-MOF (49 μg/mL)+RT (6 Gy); Group V CuFe-MOF-TPP(50 μg/mL)+RT (6 Gy). 2',7' -dichlorofluorescin diacetate (DCFH-DA) was added as an ROS probe. Fluorescence emitted was recorded using a CLSM while FCM analysis was performed to investigate the fluorescence intensity.

13. Intracellular GPX4 detection

After incubation, CT26 cells were sequentially treated with different samples (Group I: Control; Group II: RT (6 Gy); Group III: CuFe-MOF-TPP (50 μg/mL); Group IV CuFe-MOF (49 μg/mL)+RT (6 Gy); Group V CuFe-MOF-TPP(50 μg/mL)+RT (6 Gy)). After 12 hours of incubation, cells were fixed with 4.0% paraformaldehyde, permeabilized with 1.0% Triton X-100, and incubated overnight with anti-GPX4 rabbit primary antibody (dilution 1:1000). The cells were then washed with PBS and incubated for 30 minutes with an Alexa Fluor 555-labeled anti-rabbit secondary antibody. Nuclei were counterstained with DAPI. Fluorescence imaging was performed using a CLSM.

14. Evaluation of DLAT aggregation

CT26 cells were treated with different conditions including Group I: Control; Group II: RT (6 Gy); Group III: CuFe-MOF-TPP (50 μg/mL); Group IV CuFe-MOF (49 μg/mL)+RT (6 Gy); Group V CuFe-MOF-TPP(50 μg/mL)+RT (6 Gy). Similar to the pre-processing process above, cells were stained with anti-DLAT mouse antibody secondary antibody with the cell nuclei stained with DAPI. Finally, fluorescence images were captured using the LSCM.

15. Measurement of intracellular lipid peroxide (LPO) using C11-BODIPY

Following the treatment including Group I: Control; Group II: RT (6 Gy); Group III: CuFe-MOF-TPP (50 μg/mL); Group IV CuFe-MOF (49 μg/mL)+RT (6 Gy); Group V CuFe-MOF-TPP(50 μg/mL)+RT (6 Gy), C11-BODIPY581/591 was added in the medium followed by an additional 30 min incubation in the dark. Fluorescence emitted was recorded using CLSM.

16. Detection of mitochondrial membrane potential using JC-1 Staining

The JC-1 probe (10 μg/mL) was then added to each dish and incubated for 30 min.

17. Western blot of GPX4 and FDX1

After CT26 cells were treated with different samples including Group I: Control; Group II: RT (6 Gy); Group III: CuFe-MOF-TPP (50 μg/mL); Group IV CuFe-MOF (49 μg/mL)+RT (6 Gy); Group V CuFe-MOF-TPP(50 μg/mL)+RT (6 Gy), cells were collected. First the protein content was determined using the BCA Protein Assay Kit. After blocking, samples were incubated with antibodies. Protein expression levels were analyzed using ImageJ software.

18. Evaluation of immunogenic cell death

After various treatments, supernatant of cell culture medium or tumor tissues were collected and cytokines were assessed using ELISA kits according to the manufacturer's protocol. Next, 6-week-old Female Balb/c mice were purchased from Rui Mei Nuo Biotechnology Co., Ltd. Bone marrow dendritic cells (BMDCs) were extracted from Balb/c mice following the standard protocols. Then, BMDCs were co-incubated with treated CT26 and DC maturation was evaluated using FCM.

19. *In vivo* anticancer ability at tumor site

All animal procedures were approved by the Institutional Animal Care and Use Committee (IACUC) of Jilin University (Approval No.: KT202503087) and were conducted in accordance with the relevant ethical guidelines. To establish a subcutaneous tumor model, 1×10^6 CT26 cells were subcutaneously injected on the right lap of Balb/c mice aged 6 weeks. Mice were treated including Group I: Control; Group II: RT (6 Gy); Group III: CuFe-MOF-TPP (10 mg/kg of body weight); Group IV CuFe-MOF (9.8 mg/kg of body weight) + RT (6 Gy); Group V CuFe-MOF-TPP(10 mg/kg of body weight)+RT (6 Gy). Before RT conduction, each mouse was anesthetized via intraperitoneal injection of sodium pentobarbital (5 mg/kg body weight). The body weight, primary and distant tumor volumes and survival status were monitored every other day. Finally, tumors were collected and fixed in 4.0 % paraformaldehyde. GPX4, DLAT, Ki-67, Tunel immunofluorescence staining and H&E staining were performed to further evaluate the therapeutic effect of different formulations.

20. Statistical analysis

All data were presented as mean ± standard deviation and were examined with GraphPad Prism 10.1.2. n.s. represented not significance; *$p<0.05$ represented statistical significance; **$p<0.01$ represented moderate statistical significance and ***$p < 0.001$ represented highly statistical significance.

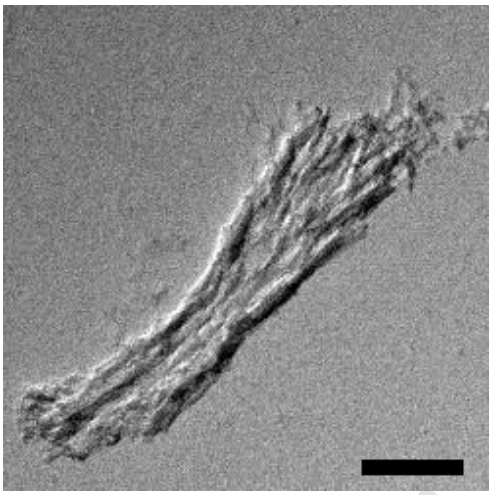

Supplementary figure 1. TEM images of CuFe-MOF. Scale bar: 500 nm.

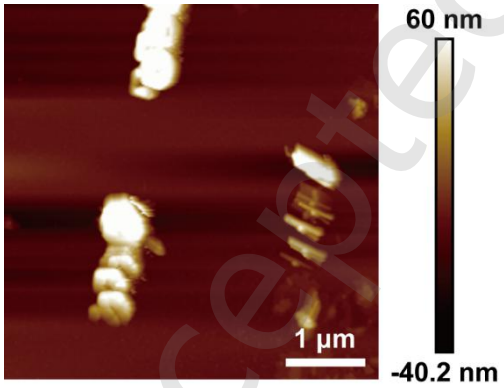

Supplementary figure 2. AFM height profiles of CuFe-MOF-TPP.

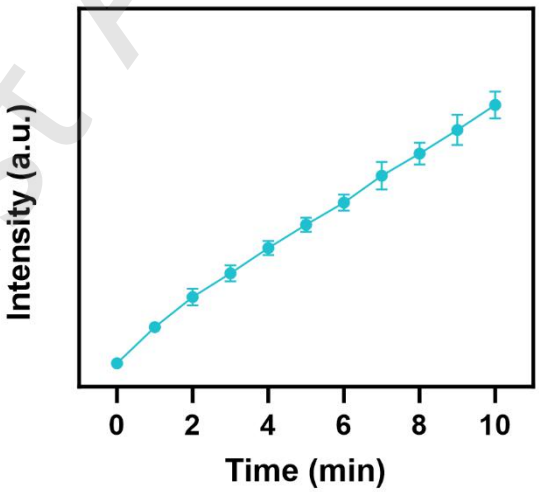

Supplementary figure 3. Absorbances at 652 nm of CuFe-MOF-TPP detected by TMB.

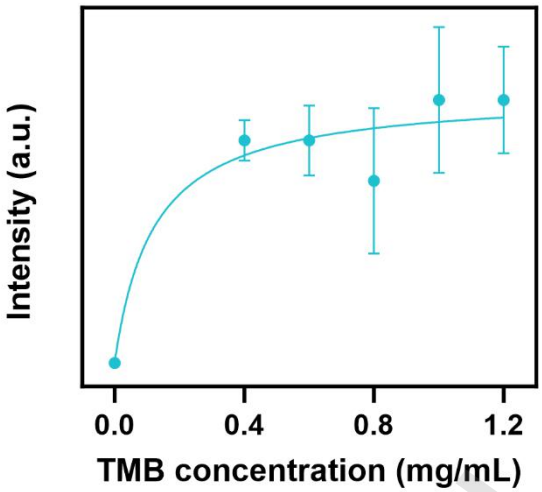

Supplementary figure 4. Absorbances at 652 nm of CuFe-MOF using TMB at various TMB concentrations.

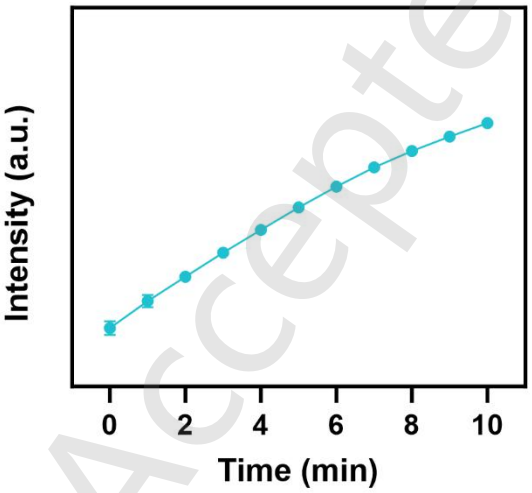

Supplementary figure 5. POD-like activities of CuFe-MOF varies with time.

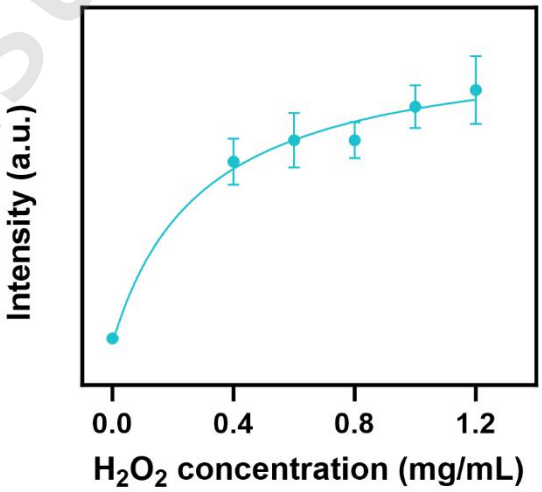

Supplementary figure 6. POD-like activities of CuFe-MOF varies with H_2O_2 concentration.

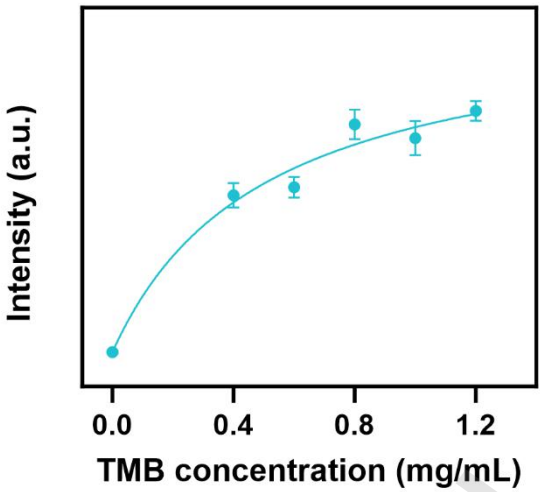

Supplementary figure 7. POD-like activities of CuFe-MOF varies with TMB concentration.

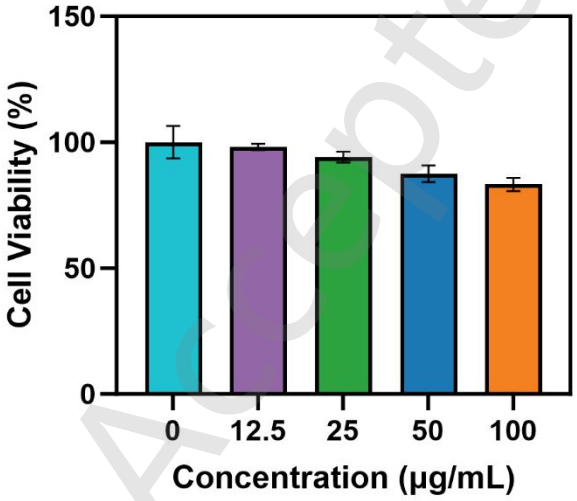

Supplementary figure 8. Cell viability of MCF-10A.

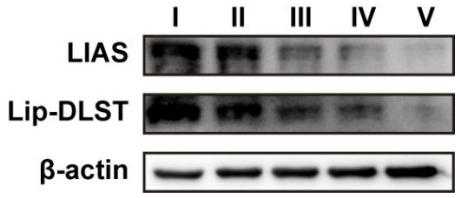

Supplementary figure 9. WB analysis of LIAS and Lip-DLST.

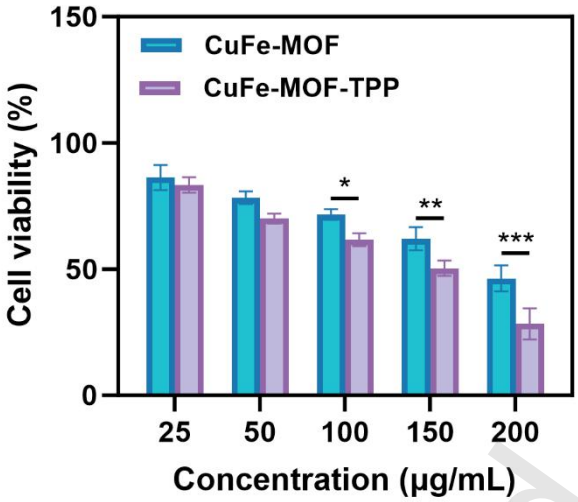

Supplementary figure 10. Cell viability assessment of MB49.

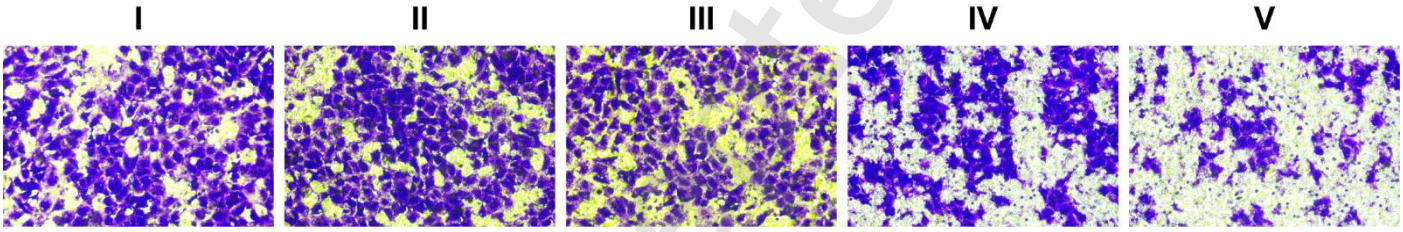

Supplementary figure 11. Representative staining of transwell assay. Group settings, I: Control, II: RT, III: CuFe-MOF-TPP; IV: CuFe-MOF +RT; V: CuFe-MOF-TPP+RT.

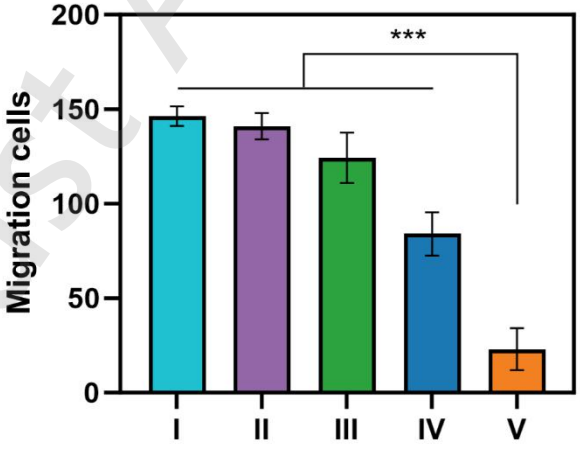

Supplementary figure 12. Migration cells quantification.

Address correspondence to Bin Liu, liub18@mails.jlu.edu.cn; Kelong Fan, fankelong@ibp.ac.cn; Min Luo, 15172327560@163.com

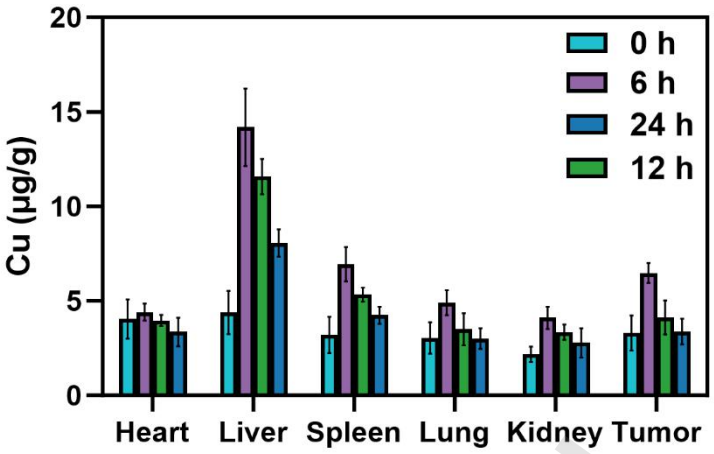

Supplementary figure 13. Biodistribution of copper ions in main organs and tumors 24 h after injection.